https://doi.org/10.1139/cgj-2018-0505

Effects of repeated hydraulic loads on microstructure and hydraulic behaviour of a compacted clayey silt

Arash Azizi[1, 4*], Guido Musso[2] & Cristina Jommi [3,5]

*Corresponding author

1. Post-doc Researcher
Department of Structural, Geotechnical and Building Engineering
Politecnico di Torino
Corso Duca degli Abruzzi, 24
10129 Torino, Italy
arash.azizi@polito.it

2. Associate Professor
Department of Structural, Geotechnical and Building Engineering
Politecnico di Torino
Corso Duca degli Abruzzi, 24
10129 Torino, Italy
guido.musso@polito.it

3. Professor
Department of Civil and Environmental Engineering,
Politecnico di Milano
Piazza Leonardo da Vinci, 32
20133 Milano, Italy
cristina.jommi@polimi.it

4. Research Fellow
Department of Engineering
Durham University
Lower Mountjoy, South Rd.
DH1 3LE Durham, UK
arash.azizi@durham.ac.uk

5. Professor
Department of Geosciences and Engineering

Draft

Delft University of Technology
Stevin weg 1
2628CN Delft, The Netherlands
c.jommi@tudelft.nl

Draft

Abstract

Soils used in earth constructions are mostly unsaturated, and they undergo frequent drying-wetting cycles (repeated hydraulic loads) due to changes in climatic conditions or variations of the ground water level, particularly at shallow depths. After compaction, changes in water content can significantly influence the hydromechanical response of the construction material, which therefore has to be assessed for repeated hydraulic loads. This research investigates the effect of such loads on the microstructure and hydraulic behaviour of a silty soil, typically used in the construction of embankments and dykes, with the aim of providing a better understanding of the consequences of drying-wetting cycles on the response of the material over time. Experimental tests were performed to study the impact of drying-wetting cycles on the water retention, hydraulic conductivity and fabric of compacted specimens. Fabric changes are documented to take place even without significant volumetric strains, promoting an irreversible increase in the hydraulic conductivity and a reduction in the capacity to retain water compared to the as-compacted soil. The fabric changes are interpreted and quantified by means of a hydromechanical model, which accounts for the evolving pore size distribution at different structural levels. The proposed model reproduces quite well the microstructural observations, together with the evolution of the water retention behaviour and of the hydraulic conductivity.

Draft

Key words:

Compacted silt; drying-wetting cycle; water retention; hydraulic conductivity; microstructure; hydromechanical model

Number of words: 7350
Number of figures: 13
Number of tables: 6

1. Introduction

Earth structures are widely exposed to interactions with the environment, especially to variations in the atmospheric conditions and in the ground water level. When the environmental conditions become severe, failure of these structures may occur causing economic losses and casualties. Far from failure, atmospheric changes and water level oscillations constitute repeated hydraulic loads inducing drying-wetting cycles, which significantly affect the geotechnical behaviour of earth structures and slopes because of their impact on the distribution of water pressure (e.g. Vaughan et al., 2004; Smethurst et al. 2006; Rouainia et al., 2009).

Soil-atmosphere interactions are mainly due to precipitations and to seasonal variations of air relative humidity and temperature. These processes may lead to substantial changes in soil water content and suction, particularly within superficial soil layers (e.g. Croney, 1977; Albright et al., 2004; Smethurst et al., 2006). Calabresi et al. (2013) monitored the suction and the water content within a soil embankment at Viadana, along the Po River in the North of Italy. In proximity of the phreatic surface, a zone deeply influenced by the level of impounded water and by capillarity phenomena, very small variations in suction and moisture content occurred. Instead, suction and water content oscillated between extreme values in superficial layers, mainly due to Relative Humidity (*RH*) changes in air (between 30 % and 100 %) during the inspection time period (April to October 2001). Such *RH* oscillations represent hydraulic loads that can significantly influence the efficiency of dykes, embankments and also of covers of waste contaminant landfills consisting of soils compacted with high compaction efforts (e.g. Daniel, 1987). Benson et al. (2007) characterized the hydraulic behaviour of soils used for water balance covers at the time of construction and a few years after placement. Over time, generally the hydraulic conductivity increased and the air entry value decreased. Similar effects on the hydraulic behaviour of unsaturated soils have been related to desiccation cracks (Drumm et al. 1997; Albrecht and Benson, 2001), to freeze-thaw cycles (Benson et al., 1995; Chapuis, 2002), and to plant root growth (Smethurst et al. 2006). For all cases, the detected changes in the hydraulic behaviour suggest void ratio and/or fabric evolution.

The assessment of the long-term behaviour of low activity compacted soils is fundamental to properly understand and predict the performance of geotechnical structures, such as dykes and embankments, which are mostly built with these materials. However, little attention has been paid to the effects of hydraulic loading on the fabric and hydraulic behaviour of low activity compacted soils, while many works have studied these effects for compacted soils of moderate to high activity (e.g. Sharma, 1998; Alshihabi et al., 2002; Cui et al., 2002; Fleureau et al., 2002; Lloret et al., 2003; Alonso et al., 2005; Cuisinier and Masrouri, 2005; Nowamooz and Masrouri, 2009; Airò Farulla et al., 2010; Romero et al., 2011). This paper aims to investigate the evolution of the hydraulic behaviour and of the microstructure of a low activity silty soil exposed to drying-wetting cycles such as those expected to act on superficial soil layers in temperate climates.

Draft

2. Soil properties

The tested soil, collected at Viadana (North Italy), is a clayey silt (grain size distribution in Fig. 1) and it was used in the construction of an experimental embankment for the assessment of earth structures aimed at the containment of floods along the Po river. The same material has been previously studied by different authors (e.g. Nocilla et al., 2006; Vassallo et al., 2007; Calabresi et al., 2013; Azizi et al., 2017).

The soil retrieved from different places on site can contain different percentages of clay and sand. The Atterberg limits, grain specific gravity, calcite content, and grain size distribution of the Viadana silt samples used in this investigation are listed in Table 1. The material can be classified as low plasticity silt (ML) according to ASTM D2487, with a plasticity index equal to $PI = 8.3\%$. The activity index is $A = 0.4$, a value typical of low activity soils.

According to X-ray diffraction, the main mineralogical constituents are quartz, calcite and clay minerals of low to moderate activity (mainly kaolinite, chlorite and illite).

3. Specimen preparation and drying-wetting cycles

The collected material was dried and mechanically ground. The specimens were prepared by statically compacting the soil at a dry density $\rho_d = 1680$ kg/m^3 and at a gravimetric water content $w = 20$ %. For each specimen, the dry soil powder was initially sprayed and hand-mixed with demineralised water according to the target water content, sealed in plastic bags and kept hanging over distilled water in a sealed humid container for 48 hours allowing water content equilibration. The wet soil was then placed in a rigid ring having a diameter of 50 mm. An axial force was gradually applied until the desired height (20 mm) was achieved. To avoid the generation of excess pore pressure that might affect homogeneity, a low rate of axial displacements (0.15 mm/min) was imposed during loading. After compression, the specimen was sealed with an impermeable plastic film and kept hanging over distilled water in a closed container for the following 24 hours to allow for water content equilibration. No significant water content changes occurred during this stage. The water content and the dry density of the specimens are similar to those adopted in situ for the experimental embankment (Rojas et al., 2010).

Six specimens were used to characterise the microstructure and to study the hydraulic behaviour after compaction. Their dry density (ρ_d), water content (w), void ratio (e), degree of saturation (S_r) and suction (s) are reported in Table 2. Other eight specimens were used to study the effects of repeated hydraulic loads on the water retention, hydraulic conductivity and microstructure. These specimens were subjected to 3 and 6 drying-wetting cycles, namely, "3D/W" and "6D/W" ~~(or generally "D/W")~~. Drying was imposed by placing the specimens within the holder ring above a rigid mesh. Evaporation of water occurred across the mesh and towards the laboratory environment, at controlled temperature and relative

Draft

humidity. The temperature was T = 21°C (± 0.5 °C). The relative humidity was double-checked and measured to be around RH = 38.5% (the combination of relative humidity and temperature corresponds to a total suction ψ = 129 MPa according to the psychrometric law). The weight and the height of the specimens were measured to track changes in water content and volume. For each of the drying steps, the water content decreased until equilibrium was established after about 120 hours, reaching the same value of w = 0.38 % at the end of all cycles. During drying, an axial stress of 10 kPa was applied. No significant radial strains were induced and shrinkage of the specimen occurred uniaxially. ~~(for weight measurements to be taken, the specimens being held only by the ring were moved back and forth from the mesh to a high precision scale).~~

Wetting took place in the same mould used for static compaction, through a plastic porous disc at the bottom, which was connected to a water pressure line to introduce water into the specimen. ~~An injection rate of 0.5 cm³/h was imposed.~~ A small pressure head of 5 kPa was imposed to maintain the pressure gradient adequately low, thus minimising possible effects of transient high water pressures on the soil volume and microstructure. Water filled the pores gradually while the air was escaping through a tiny passage conduit at the top of the mould. The mass of water injected was measured with a water volume indicator and the average injection rate was about 500 mm³/h. Wetting was stopped when the water content of the specimens was equal to the one at compaction (w = 20%). Vertical displacements were allowed during wetting while radial ones were constrained by the holder ring. After the drying-wetting cycles, the specimens were wrapped up in plastic bags and kept hanging over distilled water in a closed container for at least 5 days to ensure water content homogenization. The size of each specimen was then measured. Fig. 2 shows the evolution of water content with time along one drying-wetting cycle.

The filter paper technique was used to measure suction after compaction and after the drying-wetting cycles. The calibration curve of Leong et al. (2002) was adopted. ~~Although the filter paper technique is claimed not to be precise in the low suction range,~~ The measurements were very consistent with the water retention data of these specimens (see section 5.1 for comparison). The average measured suction of as-compacted specimens was s = 33 kPa, whereas the one of 6D/W specimens was s = 5 kPa.

3.1 Mechanical response during drying-wetting cycles

Fig. 3 shows the volume strains ε_v and water content w of the 3D/W and 6D/W specimens as a function of the number of cycles. First drying caused a relatively small shrinkage. The contractive volumetric strains at the end of drying increased during the first two or three cycles, implying some irreversible volumetric strains, and they were almost constant at the end of the following cycles during which the specimens showed nearly reversible behaviour. Negative strains (expansion)

Draft

were evident at the end of the first wetting stage, despite the water content being the same as preparation. The expansion strains also stabilized after three cycles. ~~However, the expansion volumetric strains at the end of the wetting stages consistently decreased during the following two or three drying-wetting cycles, approaching a value of zero after the third cycle.~~

4. Experimental methods

The hydraulic behaviour and the fabric evolution were studied by different tests, using the techniques summarised in Table 3. Water Retention Curves (WRC) were determined imposing matric suction s with the axis translation technique ($s \leq 400$ kPa) and imposing total suction ψ with the vapour equilibrium technique ($\psi \geq 3$ MPa). The axis translation technique was adopted in a suction controlled oedometer, where an axial net stress $\sigma_{net} = 50$ kPa was applied. A sequence of matric suction s = 10, 50, 200, 300, 350 and 400 kPa was imposed over drying. The specimens were then removed from the oedometer and placed in a desiccator with saturated salt solutions, whose total suctions at the laboratory temperature were measured with a WP4 Dewpoint Potentiometer. The following total suctions were imposed: $\psi = 3.6$, 8.8, 21.8, 40.1 and 82 MPa (using the saturated K_2SO_4, KNO_3, KCl, $NaNO_3$ and $Ca(NO_3)_2$ 4 H_2O solutions, respectively). An axial net stress of 20 kPa was imposed during this phase. For each imposed ψ, the specimens were kept in the desiccator until equilibrium was established. Their weight and volume were sequentially measured. After equilibrium at $\psi = 82$ MPa, wetting was induced by imposing the same suctions of the drying path in reversed order. The water retention data are hereby presented in terms of matric suction. The matric suction s was obtained as the difference between the total suction ψ and the osmotic suction π for each stage where the vapour equilibrium technique was applied. The osmotic suction was evaluated as follows: one specimen at the initial water content and void ratio was squeezed (Iyer, 1990) to expel a mass of pore water sufficient for electrical conductivity measurements. The electrical conductivity of the pore water was E.C. = 3.70 mS/cm, which is consistent with a molarity M = 0.039 mol/l of a NaCl solution. For each stage of the Vapour Equilibrium path, the actual molarity was evaluated assuming that only water evaporates, so that the ratio of the dissolved salt mass to the solid fraction of the soil remains constant. This molarity was converted into electrical conductivity - accounting for the decrease of the mobility of ions in concentrated solutions. For each stage, π was related to the estimated electrical conductivity through the graph reported by Fredlund and Rahardjo (1993) (originally from USDA Agricultural Handbook, 1950), which was fitted with the relationship $\pi = 31.9 \times E.C.^{1.07}$ (units kPa and mS/cm). The empirical relationship between the osmotic suction and the water content for the tested specimens was then found to be $\pi = 70.29 \times w^{-1.06}$ (w is non-dimensional).

Draft

The hydraulic conductivity of the saturated specimens was obtained by means of constant head permeability tests. The specimens were saturated by injecting water while the hydraulic head was kept constant until a steady flow of water took place. The hydraulic conductivity in unsaturated conditions was determined by back analysis of the water content changes measured during the water retention tests.

Insights on the fabric of specimens at different states were provided by Pore Size Distributions (PSD) curves and by direct observations with Environmental Scanning Electron Microscope (ESEM) pictures. The PSD curves were determined through Mercury Intrusion Porosimetry (MIP) carried out using a Micromeritics AutoPore IV 9500, in which two different systems were operated: a low mercury pressure system (between 0 and 0.345 MPa) and a high mercury pressure system (between 0.345 MPa and 228 MPa). These operating systems allow mercury to intrude pores with radii ranging between 0.0035 µm and 200 µm. Cylindrical specimens with height and diameter of 10 mm were trimmed from the original ones for MIP analyses. The fabric of the wet specimens was preserved by dehydration using the freeze-drying technique (Delage and Pellerin, 1984). All specimens were then weighted and placed in the penetrometer, followed by evacuation of gas from the chamber to generate the vacuum condition.

5. Effects of repeated hydraulic loads on the hydraulic behaviour

5.1 Water retention behaviour

Fig. 4(a) shows the water retention curves of the as-compacted specimens and of the specimens subjected to drying-wetting cycles in terms of log(s)-S_r. A reduced capacity for retaining water of the D/W specimens was evident along both the main drying and the main wetting paths, where the water content of the D/W specimens was always noticeably smaller than that of the as-compacted specimen for suction s < 20 MPa. Drying–wetting effects were not observed at very high suction ($s \geq 20$ MPa). Consistently with the reversible mechanical response after the third drying-wetting cycle, the drying WRC of the 6D/W specimen was quite similar to the one of the 3D/W specimen. Volume changes taking place during the water retention tests were very small.

The initial void ratio of the D/W specimens was slightly smaller than the one of the as-compacted specimens because the formers had a slightly higher volume decrease under the axial net stress σ_{net} = 50 kPa imposed in the suction controlled oedometer. Volume changes taking place during the water retention tests were very small (Fig. 4(b)). Altogether, the results showed that the water retention behaviour of the D/W specimens differs from the original one mainly because of changes in the soil fabric, mostly occurring during the first cycles, rather than because of changes in the void ratio.

Different water retention domains can be identified: a high suction range with almost no hysteresis ($s \geq 20$ MPa), an intermediate suction range and a low suction range, which can be distinguished from each other by substantial changes in the shape of the curves as shown in Fig. 4(c) in terms of water ratio ($e_w = S_r.e$) and suction. The size of the two latter

Draft

domains, which are separated by the inflection point of the WRC, evolved during the drying-wetting cycles (see also Romero and Vaunat, 2000; Aubertin et al., 2003; Romero et al., 2011; Della Vecchia et al., 2015).

5.2 Hydraulic conductivity

The average saturated hydraulic conductivity of the specimens, evaluated by constant head tests, was $K_s = 1.1\times10^{-9}$ m/s for the as-compacted specimens and $K_s = 1.3\times10^{-8}$ m/s for the 6D/W specimens. The hydraulic conductivity in unsaturated conditions was determined by back analysis of the water content changes measured during the water retention tests. The Finite Element code COMSOL was used to reproduce the water outflow along the suction equalization phases of the drying paths (in the range $10 \le s \le 400$ kPa) and the hydraulic conductivity was then obtained relying on Richard's equation (e.g. Eching et al. 1993; van Dam et al. 1994; Fujimaki & Inoue 2003):

$$\frac{\partial\theta}{\partial t} = -\frac{\partial}{\partial z}\frac{K_w(S_e)}{\gamma_w}\left[\frac{\partial s}{\partial z} - 1\right] \quad (1)$$

where γ_w is the specific weight of water, $\theta = \frac{e_w}{1+e}$ is the volumetric water content, z is the spatial coordinate, t is the time and K_w is the hydraulic conductivity in unsaturated conditions. The effective degree of saturation S_e is defined as $S_e = \frac{S_r - S_{res}}{1 - S_{res}}$, where S_{res}=0.07 is the residual degree of saturation. For each suction increment, the decrease in water content was expressed in terms of moisture capacity $C(s) = \frac{\partial\theta}{\partial s}$ determined from the WRC and the current hydraulic conductivity was approximated with its average constant value. The following equation was then solved:

$$C(s)\frac{\partial s}{\partial t} = -\frac{K_w(S_e)\partial^2 s}{\gamma_w \quad \partial z^2} \quad (2)$$

An optimization procedure was implemented to determine the best values of K_w for the as-compacted and 6D/W specimens. In the experiments, the water flow rate depended also on the impedance of the bottom porous stone, through which the flow took place. Therefore, the porous stone, having height 7 mm and saturated hydraulic conductivity 1.21×10^{-9} m/s, was also modeled. In the numerical simulation, suction values were imposed at the bottom of the porous stone, while a no flow condition was imposed at the top boundary.

Fig. 5(a) compares the changes in the volumetric water content $\Delta\theta$ measured during the test with the numerical predictions. According to the back analysis, the hydraulic conductivity of the 6D/W specimen is greater than the one of the as-compacted specimen over the whole saturation range (Fig. 5(b)). This general increase of hydraulic conductivity, observed also at full saturation, is related to the fabric changes taking place at almost constant volume, which are discussed in detail in the following.

Draft

6. Effects of repeated hydraulic loads on microstructure

6.1 Fabric arrangement

ESEM pictures of the as-compacted and 6D/W specimens shown in Figs. 6(a), 6(b) and 6(c) portray the soil fabric and the pore network. These pictures were taken while setting the temperature T= 10 °C and the vapour pressure u_v = 630 Pa in the chamber, with a corresponding relative humidity R.H.= 53%. The silt and clay fractions are well evident. The clay fraction consists of single clay particles (denoted by 'C') and of aggregations of clay particles (clay peds). Silt particles (denoted by 'S') are also evident.

The radii of the pores between peds and between large particles and peds, recognised at the lower magnification of Figs. 6(a), 6(b) and 6(d), are of the order of a few microns. The radii of the pores within the peds appear to be clearly below 1 μm including those recognised at the higher magnification of Fig. 6(c) and those unvisible at this magnification. This may suggest three classes of pores including micropores and mesopores inside the peds and macopores external to the peds, as it will be discussed in the next section.

Fig. 6(d) shows an ESEM image of the 6D/W dry specimen. This figure shows that single peds might break into smaller peds, separated by fractures having the size of macropores, which suggests that drying-wetting cycles induce breakage of peds, increasing the macroporosity. Nonetheless, neither cracks nor fissures at the surface of the specimens were evident to the naked eye.

Draft

6.2 Pore size distribution

The pore size distributions presented in Fig. 7(a) describe the following four conditions: As-compacted (w = 20%), after first drying ('As-compacted dry', w = 0.38%), at the end of the sixth drying stage ('6D/W dry') and at the end of the sixth wetting stage ('6D/W'). The PSD curves are clearly bi-modal, with a dominant peak in correspondence of a pore radius smaller than 1 μm and another peak in the range of 5-10 μm. Microstructural changes from the as-compacted condition to the 6D/W condition are evident. The as-compacted and the as-compacted dry specimens have a dominant pore radius r = 609 nm, but the size of the peak is greater for the dry specimen. The PSDs of the 6D/W dry and 6D/W specimens overlap very well, both showing an increase of the dominant pore radius to r = 917 nm. The radius of the smaller PSD peak shifts from about 5 μm (as-compacted) to about 8 μm (wet state of the 6D/W), while it remains about 5 μm for the 6D/W dry. The evolution of the PSDs shows that the soil fabric is sensitive to repeated hydraulic loads, confirming that fabric changes take place even without significant changes in the total volume.

The total intruded void ratio e_{int} was smaller than the total void ratio e (Fig. 7(b)) since not all the available porosity was intruded by mercury. This difference is due both to very large pores, filled by mercury at very low pressures, whose

volume is not measured during intrusion, and to very small pores which are not intruded even at very high pressures. The fraction of void ratio associated to the very small pores is assumed to be equal to the water ratio corresponding to irreducible saturation, and it is about 0.04 for all specimens. The non-intruded fraction of void ratio associated with very large pores is then estimated as the difference between the non-intruded void ratio and 0.04.

Based on the PSDs, three classes of pores (micropores, mesopores and macropores) are identified. This allows individuating a microstructural void ratio e_{Mi}, a mesostructural void ratio e_{Me} and a macrostructural void ratio e_{Ma}:

$$e_{Mi} = \frac{V_{vMi}}{V_s},\ e_{Me} = \frac{V_{vMe}}{V_s},\ e_{Ma} = \frac{V_{vMa}}{V_s} \tag{3}$$

where V_{vMi} is the volume of the micropores, V_{vMe} is the volume of the mesopores, V_{vMa} is the volume of the macropores and V_s is the volume of the solid phase. The total void ratio e is then:

$$e = e_{Mi} + e_{Me} + e_{Ma} \tag{4}$$

Selecting a criterion to discriminate between different classes of pores always involves some degree of arbitrariness, and the choices that were made in the elaboration of the data are presented here. Micropores are defined as those pores still saturated at very high suctions, and whose behaviour during drying-wetting cycles is completely reversible. On the basis of the results in Fig. 4(c), the corresponding void ratio is e_{Mi} = 0.06 for all conditions. The threshold pore radius separating micropores from mesopores R_{Mi} is determined as the radius at which the following condition is satisfied:

$$e_{Mi} = \int_{3.5}^{R_{Mi}} \frac{PSD(r)}{r.\ln(10)}.dr + 0.04 \tag{5}$$

where 3.5 nm is the smallest pore radius intruded by MIP and *0.04* is the void ratio corresponding to the very small non intruded pores. By imposing e_{Mi} = 0.06 it follows R_{Mi} = 11 nm. Note that the argument function of the integral in eq. (5) follows logically from the definition of the PSD as the incremental fraction of intruded void ratio with respect to the logarithm of the pore radius, as discussed for instance by Della Vecchia et al. (2015).

Mesopores are identified with the larger pores within the clay peds. According to the ESEM pictures (Fig. 6), their radii are expected to be smaller than 1 μm. MIP analyses of specimens loaded to increasingly higher net stresses showed a progressive reduction of the volume of the pores having radii greater than the dominant peak, and no clear effects on pores whose radius was smaller (Azizi et al., 2018). The evidence confirms the shared view that mechanical compression mostly affects pores external to clay aggregates (or macro-pores, see e.g. Delage and Lefebvre 1984; Tarantino and De Col, 2008, Koliji et al., 2010). Therefore, the threshold pore radius R_{Me} separating the macropores from the mesopores was selected as the pore radius of the dominant peak of the PSD (equal to 609 nm for the as-compacted and first drying states, and equal to 917 nm for the 6D/W dry and 6D/W wet states). V_{vMe} is the volume of pores whose entrance radius is

Draft

between R_{Mi} and R_{Me}; the values of e_{Me} were obtained through Eq. (3). Finally, values of e_{Ma} for each state were determined by applying Eq. (4).

The threshold pore radii separating the different classes of pores and the void ratios e_{Mi}, e_{Me} and e_{Ma} are summarised in Table 4.

6.3 Fabric evolution based on conjugate analysis of MIP and ESEM data

Repeated hydraulic loads induce two different effects at the mesostructural level. Firstly, the mesostructural void ratio of the 6D/W states (e_{Me} = 0.32) is smaller than the one of the as-compacted state (e_{Me} = 0.36). This suggests that the peds experience irreversible strains, and their contraction during drying is not fully recovered during wetting. Since the final suction is smaller than the one at preparation, the behaviour of the peds cannot be elastic, otherwise drying-wetting cycles would lead to a net expansion of the peds. Secondly, the radius of the larger mesopore increases from 609 nm to 917 nm (Table 4).

While the overall void ratio remains constant upon the repeated hydraulic loads, the macrostructural void ratio evolves from the initial e_{Ma} = 0.24 of at the as-compacted state to e_{Ma} = 0.28 of the 6D/W wet state. Simultaneously, the dominant radius of macropores increases from 5030 nm to 8230 nm. Contraction of the peds is responsible for larger macroporosity and larger individual macropores, thanks to stiffening effect of the granular silt skeleton, which is less sensitive to water content changes (as observed also for Barcelona clayey silt by Romero et al., 2014). The lower air entry value of the peds, the larger macrostructural void ratio and the larger pore radii of the macrostructure of 6D/W samples all concur to explain the significant change of the water retention capacity and the increase in hydraulic conductivity.

The experimental WRCs and those predicted on the basis of MIP results are compared in Fig. 8. Since mercury is a non-wetting fluid, MIP data can be used to derive a water retention curve by assuming that its penetration is equivalent to air intrusion during a drying path. The diameter r of a pore determines both the matric suction s during drying and the pressure of penetrating mercury p (e.g. Romero et al., 1999), so that:

$$s = \frac{4\sigma cos\theta_w}{r}; p = -\frac{4\sigma_{Hg} cos\theta_{Hg}}{r}; s = -\frac{\sigma cos\theta_w}{\sigma_{Hg} cos\theta_{Hg}} p \approx 0.196\, p \qquad (6)$$

where σ = 0.072 N/m is the surface tension of water and θ_w = 0° is the contact angle for the air-water interface, σ_{Hg} = 0.484 N/m is the surface tension of mercury and θ_{nw} = 140° is the contact angle between mercury and the particle surface. The WRC is derived from MIP data at the fixed void ratio of the tested sample. On the contrary, single values of water retention determined experimentally over drying/wetting paths reflect the concomitant shrinkage and swelling occurring during the test. Direct comparison of the two is hardly significant in the case of active clays (Romero et al., 2011), for

Draft

345 which numerous PSDs are required to determine the complete retention domain (Della Vecchia et al., 2015). However,
346 in the case of Viadana silt changes in total void ratio are negligible, and the MIP derived WRCs reproduce quite well the
347 experimental water retention both along first drying and along drying after 6D/W cycles. The difference between the first
348 drying and the following drying paths shows the relevance of internal microstructural rearrangement for the tested silty
349 soil, though its composition include no relevant percentage of active clay minerals particularly sensitive to physico-
350 chemical phenomena.
351

352 **7. Modelling macroscopic behaviour accounting for microstructural evolution**
353 **7.1 Coupled hydromechanical model**

354 The experimental results show that both the hydraulic behaviour and the fabric of Viadana silt evolve with drying-wetting
355 cycles. The volume of the peds and the water retention properties undergo irrecoverable changes during the first cycle,
356 and stabilise afterwards. To assist in the interpretation of the data and to quantify the effects of the drying-wetting cycles,
357 a microstructural framework is needed. Table 4 suggests that the microstructural void ratio e_m remained constant, so it is
358 not strictly necessary to consider the micro-pores separately from the meso-pores when formulating a microstructural
359 model, since both classes of pores are found within the peds. A double porosity framework was then used which allows
360 to distinguish between the micro-meso and the macro fabric levels and to incorporate microstructural changes.
361 A model for the volumetric response is introduced to this extent. Two structural levels are defined and described based
362 on their respective void ratios, one pertaining to the void space within the peds (intra-peds) and the other external to the
363 peds (macrostructure). The overall behaviour of the material follows as the superposition of the two structural levels
364 where the two fabric levels are assumed to be in hydraulic and mechanical equilibrium. Two sets of hydromechanical
365 variables are defined: matric suction and Bishop type effective stress as stress variables, and water ratio (or degree of
366 saturation) and volume strain (or void ratio) as strain variables. The proposed model shares fundamental hypotheses with
367 double porosity models formulated for expansive soils (e.g. Gens & Alonso, 1992; Alonso et al., 1999; Mašin, 2013,
368 Musso et al., 2013) whereas it adopts the elastoplastic framework for the behaviour of the peds based on the
369 microstructural observations. The asymptotic behaviour resulting from an increasing number of drying-wetting cycles is
370 then reproduced as a direct consequence of the proposed hardening laws, which are discussed in the following.
371

372 **7.1.1 Fabric levels and strain variables**

373 Micropores and mesopores belong to the intra-peds porosity, while macro-pores are associated with the porosity external
374 to the peds. The intra-peds void ratio e_m and the macrostructural void ratio e_{Ma} are defined as:

Draft

$$e_m = e_{Me} + e_{Mi} = \frac{V_{vMe} + V_{vMi}}{V_s} = \frac{V_{vm}}{V_s}, e_{Ma} = \frac{V_{vMa}}{V_s} \quad (7)$$

where V_{vm} is the volume of the intra-peds voids.

The intra-peds water ratio e_{wm} and the macrostructural water ratio e_{wMa} are obtained imposing that the total mass of water stored within the soil is the sum of the mass of water within the peds and the mass of water in the macroporosity:

$$e_w = e_{wMa} + e_{wm} = e_{Ma}S_{rMa} + e_mS_{rm} \quad (8)$$

with $e_{wm} = \frac{V_{wm}}{V_s}$, $e_{wMa} = \frac{V_{wMa}}{V_s}$, $S_{rm} = \frac{V_{wm}}{V_{vm}}$, $S_{rMa} = \frac{V_{wMa}}{V_{vMa}}$, where V_{wm} is the volume of water within the peds, V_{wMa} is the volume of water within the macropores, S_{rm} is the intra-peds degree of saturation, S_{rMa} is the macrostructural degree of saturation.

7.1.2 Stress variables

Two stress variables are employed including a mechanical constitutive stress and suction. The first one is assumed to depend on the net stress (σ_{net}), the effective degree of saturation (S_e) and the suction in the form:

$$\boldsymbol{\sigma}' = \boldsymbol{\sigma}_{net} + S_e s\boldsymbol{I} \quad (9)$$

Draft

where Eq. (9) is a general expression, which can be used to describe the average mechanical stress acting on the soil skeleton or on each structural level (macrostructural stress σ'_{Ma} or peds stress σ'_m), by using the corresponding effective degree of saturation. As in most of the previous double porosity models, the total (net) stress acting on each level is assumed to be the same (e.g. Alonso et al., 1999; Mašin, 2013; Wang et al., 2015). The second stress variable is the matric suction. Similar stress variables have been adopted by different authors (e.g. Jommi 2000; Romero and Jommi, 2008; Della Vecchia et al., 2013).

7.1.3 Water retention model

According to Eq. (8), the overall WRC in terms of water ratio $e_w(s)$ is expressed as the superposition of the WRCs of the two fabric levels (e.g. Durner, 1994; Casini et al., 2012; Della Vecchia et al., 2015):

$$e_w(s) = e_{Ma}\left[\frac{1}{1 + (\alpha_{Ma}s)^{n_{Ma}}}\right]^{m_{Ma}} + e_m\left[\frac{1}{1 + (\alpha_m s)^{n_m}}\right]^{m_m} \quad (10)$$

where n_{Ma}, m_{Ma}, α_{Ma} and n_m, m_m, α_m are the parameters of the van Genuchten's model (1980) for macro-pores and intra-peds pores, respectively. The total degree of saturation is obtained by the sum of S_{rMa} and S_{rm} weighted by the corresponding volumetric fractions.

399 A relationship between water ratio and suction in the scanning domain is needed for the simulation of the transition from
400 drying to wetting branches (and vice versa) over the hydraulic cycles. The incremental form of equation (10) reads:

$$de_w(s) = de_{wMa} + de_{wm} = [S_{rMa}de_{Ma} + e_{Ma}dS_{rMa}] + [S_{rm}de_m + e_m dS_{rm}] \quad (11)$$

401

402 The scanning curves are predicted by replacing $dS_r = -k_{sc}ds$ for each structural level:

$$de_w^{sc}(s) = \left[\frac{e_{wMa}}{e_{Ma}}de_{Ma} - e_{Ma}k_{sc}ds\right] + \left[\frac{e_{wm}}{e_m}de_m - e_m k_{sc}ds\right] \quad (12)$$

403 where k_{sc} controls the slope of the scanning curves. The behaviour in the scanning domain is assumed to be reversible.

404

405 **7.1.4 Mechanical model**

406 Water retention depends on the macrostructural and intra-peds void ratios, whose evolution is predicted by a mechanical
407 model. Wheeler et al. (2003) proposed an elastoplastic framework that couples hydraulic hysteresis with stress-strain
408 behaviour. A similar framework is adopted to reproduce the mechanical behaviour of the peds coupled with the intra-
409 peds water retention. The peds constitutive stress (σ'_m) is employed to predict the volumetric changes of the peds,
410 influenced by the intra-peds effective degree of saturation. On the other hand, intra-peds void ratio changes affect the
411 intra-peds water ratio, because both the water storage capacity and the air-entry value evolve.

412 Hardening is introduced including two yielding criteria: one associated with mechanical straining of the peds and the
413 other responsible for irreversible changes of the peds water ratio. As shown in Fig. 9(a), the former yielding occurs when
414 the stress path reaches the loading collapse (LC) curve whereas the latter is triggered if the stress path reaches the suction
415 increase (SI) curve during drying, or the suction decrease (SD) curve during wetting. These yield curves are expressed
416 as:

$$\text{LC: } \sigma'_m = \sigma'^*_m, \text{ SI: } s = s_I, \text{ SD: } s = s_D \quad (13)$$

417

418 Where σ'^*_m is the peds yield stress, s_I is the suction increase yield curve and s_D is the suction decrease yield curve.
419 Increments of volumetric strains of the peds occurring inside the elastic domain ($\Delta\varepsilon^e_m$) are given by:

$$d\varepsilon^e_m = \frac{\kappa_m d\sigma'_m}{(1+e_m)\sigma'_m} \quad (14)$$

420

421 where κ_m is the elastic compliance for the intra-peds void ratio. For stress paths within the elastic domain, the degree of
422 saturation evolves along the scanning curves.
423 If yielding occurs directly on the SI, it induces water ratio changes on the main drying WRC accompanied with hardening
424 of the LC, whereas direct yielding on the SD induces water ratio changes on the main wetting WRC accompanied with

Draft

softening of the LC. If yielding occurs on the LC, it produces plastic volumetric strains with a coupled outward movement of the SI and inward movement of the SD. The SI and the SD evolve together:

$$\frac{ds_I}{s_I} = \frac{ds_D}{s_D} \tag{15}$$

When yielding occurs due to SI or SD, the hardening law is:

$$d\sigma'^{*}_{m} = h_{lC}\sigma'^{*}_{m}\frac{ds_I}{s_I} \tag{16}$$

h_{lC} controls the coupled movement of the LC due to SI or SD yielding. The increments of plastic volumetric strains ($d\varepsilon_m^p$) due to yielding of LC curve are

$$d\varepsilon_m^p = \frac{(\lambda_m - \kappa_m)d\sigma'^{*}_{m}}{(1+e_m)\sigma'_m} \tag{17}$$

where λ_m and κ_m are model parameters and the hardening law in this case is given by,

$$ds_I = h_s s_I \frac{d\sigma'^{*}_{m}}{\sigma'^{*}_{m}} \tag{18}$$

where h_S controls the coupled movement of SI and SD.

The general expression for plastic strain increment can be derived through Eqs. (16) and (17):

$$d\varepsilon_m^p = \frac{(\lambda_m - \kappa_m)}{(1+e_m)(1-h_s h_{lC})}\left(\frac{d\sigma'^{*}_{m}}{\sigma'^{*}_{m}} - h_{lC}\frac{ds_I}{s_I}\right) \tag{19}$$

Two flow rules are given, respectively associated to the yielding on the SI and SD curves:

$$\frac{d\varepsilon_m^p}{de_{wm}} = 0 \tag{20}$$

and associated to the yielding on the LC curve:

$$\frac{de_{wm}}{d\varepsilon_m^p} = 0 \tag{21}$$

Changes of the intra-peds void ratio are written in the form:

$$de_m = -d\varepsilon_m(1+e_m) = -(d\varepsilon_m^e + d\varepsilon_m^p)(1+e_m) \tag{22}$$

The influence of the mechanical effects on the WRC of the peds is shown in Fig. 9(b). The specimens were subjected to a wide range of suction and the peds were almost completely dry at the end of drying, whereas they were entirely saturated at the end of wetting. SI yielding occurred when air entered the saturated peds (suction greater than their air-entry value), and SD yielding occurred along wetting when the degree of saturation of the peds S_{rm} was greater than the residual one.

Draft

443 A similar framework may also be adopted also for the macrostructural fabric level. However, changes of the
444 macrostructural void ratio were evaluated here as the difference between the changes of the total void ratio and that of
445 the intra-peds void ratio. A simple elastic expression was used for the increments of overall volume strains ($d\varepsilon_v$):

$$d\varepsilon_v = \frac{\kappa \cdot d\sigma'}{(1+e)\sigma'} \tag{23}$$

446 where κ is the elastic logarithm compressibility. Hence, the total void ratio changes are:

$$de = -d\varepsilon_v(1+e) \tag{24}$$

447 and the macrostructural void ratio changes are:

$$de_{Ma} = de - de_m \tag{25}$$

448 Eqs. (22) and (25) give the evolution of the void ratio of macro- and intra-peds pores which contribute to the coupled
449 water retention model (Eq. (10)).
450

451 **7.2 Calibration of the parameters**

452 The parameters calibration was mostly based on independent tests with respect to the WRCs reproduced. An oedometer
453 test was used to determine the elastic compliances of the overall soil κ and the one of the peds κ_m, which were assumed
454 to have the same value of 0.003, and the preconsolidation stress imposed during compaction, σ'^{*}_{m} = 657 kPa, which
455 identifies the initial position of the LC (see details in Azizi, 2016). The initial air entry value of the peds $1/\alpha_m$ = 236 kPa
456 was determined by means of the MIP measurements, introducing the radius of the larger mesopore (r = 609 nm) into the
457 first one of Eq. 6. According to the model, the air entry value also provides the initial position of the SI, while the SD is
458 set equal to the suction imposed at the beginning of the water retention test (SD = 10 kPa). The parameters for the WRC
459 of the macro-structure were determined imposing the best fit between the experimental water ratio of the macrostructure
460 ($e_{wMa} = e_w - e_m$) along the first drying branch for suction values smaller than the air entry value of the peds (Table 5). The
461 elasto-plastic compliance λ_m was calibrated to capture the amount of contraction of the peds during the first drying stage,
462 as determined with MIP. The scanning parameter k_{sc} was calibrated upon water retention tests presented by Azizi et al.
463 (2017). The parameters h_{lC} and h_s were calibrated to obtain a reversible behaviour after three cycles.
464 The van Genuchten's parameters of both structural levels evolve along the hydraulic cycles to adequately reproduce the
465 evolution of the water retention. Simple relationships were chosen relating $1/\alpha_{Ma}$ and $1/\alpha_m$ to the saturated water ratios
466 of the macropores e_{wMa}^{sat} and of the peds e_{wm}^{sat}:

$$1/\alpha_{Ma} = (e_{Ma0}/e_{wMa}^{sat})^4/\alpha_{Ma0} \text{ and } 1/\alpha_m = (e_{wm}^{sat}/e_{m0})^{8.2}/\alpha_{m0} \tag{26}$$

467

Draft

where e_{Ma0} and e_{m0} are the initial macrostructural and intra-peds void ratios of the as-compacted specimen, and $1/\alpha_{Ma0}$ and $1/\alpha_{m0}$ are the initial air-entry values of the respective drying curves. The empirical laws described by Eq. (26) were used both for the main drying and the main wetting curves. The parameters of the mechanical model are listed in Table 6.

The model was employed to predict the final values of α_M and α_m, which determine the WRC after 6 cycles, together with the final values of the hydraulic conductivity and of the relative permeability.

7.3 Simulation of drying-wetting cycles: mechanical behaviour and water retention

The void ratio and suction measured during the water retention tests are compared to the model predictions in Fig. 10(a). Six drying-wetting cycles were simulated. The evolution of the intra-peds and macrostructural void ratios is presented in Fig. 10(b). Void ratios evaluated on basis of the MIP data are nicely captured. Adopting an elastoplastic framework for modeling the behaviour of the peds allowed properly simulating the decrease of the intra-peds void ratio and the increase of the macro-structural void ratio occurring during the first 3 hydraulic cycles.

The modelled changes in intra-peds and macrostructural void ratios rule the evolution of the water retention, whose simulation is introduced in Fig. 11.Fig. 11(a) shows the experimental results and the model predictions for the first drying and wetting cycle in terms of S_r–log(s). The predictions of the degree of saturation of the macropores and of the peds are also provided. Since different air-entry values are defined for the two structural levels, in the suction range 64 kPa < s < 236 kPa the peds are still saturated while the macro-pores are desaturating. A similar condition occurs during wetting in the suction range 8 kPa < s < 34 kPa. The changes in the WRCs of the two structural levels due to drying-wetting cycles are given in Fig. 11(b). At the end of each wetting stage, the intra-peds pores are always fully saturated, while, for the same suction, the degree of saturation of the macropores S_{rMa} decreases during the first three cycles. The water retention behaviour of the 6D/W specimens was predicted by simulating 6 drying-wetting cycles imposed to the as-compacted specimen, and it is plotted in Fig. 11(c). The good match between experimental data and predictions shows the capability of the conceptual model to reproduce the evolution of the water retention behaviour over hydraulic cycles.

Experimental water retention data of the first drying-wetting cycle and model predictions are re-plotted in Fig. 12(a) in terms of e_w–log(s). The water ratio of peds e_{wm} at the end of the first wetting is smaller than the original one, since the intra-peds void ratio reduces due to plastic strains. On the contrary, the water ratio of macropores e_{wMa} increases. During the first three drying-wetting cycles e_m progressively reduces while e_{Ma} progressively increases, affecting the air entry values of both peds and macropores (Eq. 26). Fig. 12(b) shows the experimental results and model predictions for the

Draft

6D/W specimen. For both structural domains, the water ratio at the beginning of drying and at the end of wetting is the same since the mechanical behaviour became reversible and the water retention curves cannot evolve further.

7.4 Model validation exploiting the hydraulic conductivity analysis

The hydraulic conductivity of compacted soils having bimodal pore size distribution is mainly related to the volume and distribution of the larger pores (e.g. Cuisinier et al., 2011, Romero 2013). As a result, the increase in the saturated hydraulic conductivity K_s evidenced in Section 5.2 is justified by the increase of the macrostructural void ratio and can be modeled using a Kozeny-Carman like equation based on e_{Ma} (Romero, 2013):

$$K_s = B\frac{{e_{Ma}}^5}{1+e_{Ma}} \tag{27}$$

where B = 5×10^{-6} m/s was found to adequately simulate the experimental data. The hydraulic conductivity under unsaturated condition K_w is defined as the product of a relative permeability k_r and K_s:

$$K_w = k_r K_s \tag{28}$$

The relative permeability k_r is controlled by the size of the pores and the shape of PSD. It can be predicted either from the relationships between suction and effective degree of saturation (Mualem, 1976):

$$k_r{}^{(Mualem)} = \frac{K_w}{K_s} = {S_e}^{1/2}\left[\frac{\int_0^{S_e} dS_e/s}{\int_0^1 dS_e/s}\right]^2 \tag{29}$$

or as a power law function of the degree of saturation (e.g. Bear 1972), whose exponent is often assumed equal to 3. By admitting that the contribution to flow of the intra-peds pores is negligible, it follows that:

$$k_r{}^{(Macro)} = \left(\frac{S_r - \frac{e_{wm}}{e}}{1-\frac{e_{wm}}{e}}\right)^3 \tag{30}$$

The values of S_r, e_{wm} and e given by the simulations were introduced in both Eq. (29) and Eq. (30) to obtain the predictions presented in Fig. 13(a), where they are compared to the experimental data based on the back-analysis of Richards' equation. Both expressions captured the experimental data well, although the prediction of the power law expression was found to better match the experimental results.

Draft

The evolution of K_w during hydraulic cycles is obtained by combining the hydromechanical model with Eq. (27) and Eq. (30). The predictions are compared to the data obtained by the inverse analysis of Richard's equation in Fig. 13(b), where a good match is observed. It is worth noting that since the total void ratio changed reversibly during drying-wetting cycles, the Kozeny-Carman equation, as well as any other model giving an estimate of the hydraulic conductivity based on the total void ratio, would not be able to predict any change in the hydraulic conductivity. On the contrary, the framework developed is able to predict the irreversible increase in macroporosity during drying and wetting cycles, which resulted in the observed relevant increase in the hydraulic conductivity of the investigated soil specimens.

8. Summary and conclusions

While the influence of fabric and fabric evolution on the hydromechanical behaviour of compacted active clays has been studied in detail in the recent years, its relevance on the hydromechanical behaviour of low activity clays and silts has been less explored. These materials are widely used to build earth structures exposed to intensive interaction with water and the atmosphere. Assessment of their response to environmental actions is then relevant for the long-term stability and serviceability of engineering works. This study was aimed to evaluate the impact of typical drying-wetting cycles, occurring at relatively low stresses in earth structures after compaction, on the hydraulic behaviour of a low activity compacted clayey silt used for the construction of water defenses, and to explain the observed behaviour with the aid of microstructural evidences.

While the overall volume strains were negligible and became reversible after a limited number of drying-wetting cycles, the hydraulic behaviour was dramatically affected by the hydraulic history in which water retention capacity reduced and hydraulic conductivity increased. The fabric of the tested soil consists of peds of clay particles mixed among silt grains, with larger pores external to the peds and smaller pores within the peds. Microstructural investigation, based on MIP analyses, indicated that the porosity and the volume of the peds decreased mainly during the first cycles. Meanwhile, the fraction of porosity external to the peds increased since the overall volume remained almost constant. Thus, the repeated hydraulic loads induced a sort of hydraulic fabric degradation associated to the development of larger pores.

A double porosity model, calibrated on the microstructural observations and accounting for coupling between the hydraulic and mechanical responses, was developed. An important feature of the model was introducing an elasto-plastic behaviour for the clay aggregates, which is usually neglected in similar formulations. Good reproduction of the experimental results was obtained by imposing the dependency of the water retention on the intra-peds and macrostructural void ratios, whose evolution is governed by suction and degree of saturation. Besides, the substantial change in hydraulic conductivity observed at the sample level was explained by means of the fabric changes predicted by the proposed modelling framework. As the soil tested is a low plasticity clayey silt, its behaviour is hardly affected by the

Draft

sensitivity to water of the constituent minerals, contrarily to active clays. Nonetheless, this investigation shows that the irreversible hydromechanical behaviour of the peds causes substantial changes in the water retention capacity as well as in the hydraulic conductivity of this material. These changes should be considered when the assessment of the hydromechanical behaviour of soils used in earth constructions is required for the design lifetime, since the response of the construction will not be governed only by the soil fabric at the time of compaction.

REFERENCES

Airò Farulla, C., Ferrari, A. & Romero, E. (2010). Volume change behaviour of a compacted silty clay during cyclic suction changes. *Canadian Geotechnical Journal*, 47(6), 688-703.

Albrecht, B. & Benson, C. (2001). Effect of desiccation on compacted natural clays. *Journal of Geotechnical and Geoenvironmental Engineering*, 1271, 67–76.

Albright, W. H., Benson, C. H., Gee, G. W., Roesier, A. C., Abichou, T., Apiwantragoon, P., Lyles, B. F. & Rock, S. A. (2004). Field water balance of landfill final covers. *Journal of Environmental Quality*, 336, 1–17.

Alonso, E.E., Romero, E., Hoffmann, C. & García-Escudero, E. (2005). Expansive bentonite–sand mixtures in cyclic controlled-suction drying and wetting. *Engineering Geology*, 81, 213–226.

Alonso, E.E., Vaunat, J. & Gens, A. (1999). Modelling the mechanical behaviour of expansive clay. *Engineering Geology*, 54, 173–183.

Alshihabi, O., Shahrour, I. & Mieussens, C. (2002). Experimental study of the influence of suction and drying/wetting cycles on the compressibility of a compacted soil. *Proceedings of 1st International Conference on Unsaturated Soils*, Balkema, Rotterdam, The Netherlands, pp. 541–545.

Aubertin, M., Mbonimpa, M., Bussière, B. & Chapuis, R. (2003). A model to predict the water retention curve from basic geotechnical properties. *Canadian Geotechnical Journal*, 40, 1104–1122.

Azizi, A. (2016). Effects of hydraulic repeated loads on the hydromechanical response of an unsaturated silty soil. PhD Thesis, Politecnico di Milano.

Azizi, A., Jommi, C. & Musso, G. (2017). A water retention model accounting for the hysteresis induced by hydraulic and mechanical wetting-drying cycles. *Computers and Geotechnics*, 87, 86-98.

Azizi, A., Musso, G., Jommi C. & Cosentini, R. M. (2018). Evolving fabric and its impact on the shearing behaviour of a compacted clayey silt exposed to drying-wetting cycles, Unsat2018, Hong Kong.

Bear, J. (1972). Dynamics of Fluids in Porous Materials. American Elsevier.

Benson, C. & Khire, M. (1995). Earthen covers for semi-arid and arid climates. *Landfill Closures*, J. Dunn, and U. Singh, eds., ASCE, New York, 201–217.

Benson, C. H., Sawangsuriya, A., Trzebiatowski, B. & Albright, W. H. (2007). Postconstruction changes in the hydraulic properties of water balance cover soils. *Journal of Geotechnical and Geoenvironmental Engineering*, 133(4), 349–359.

Bishop, A. (1959). The principle of effective stress. Tecnisk Ukeblad, 39, 859–863.

Calabresi, G., Colleselli, F., Danese, D., Giani, G. P., Mancuso, C., Montrasio, L., Nocilla, A., Pagano, L., Reali, E. & Sciotti A. (2013). A research study of the hydraulic behaviour of the Po river embankments. *Canadian Geotechnical Journal*, 50, 9, 947-960.

Casini, F., Vaunat, J., Romero, E. & Desideri, A. (2012). Consequences on water retention properties of double-porosity features in a compacted silt. *Acta Geotechnica*, 7(2), 139–150.

Chapuis, (2002). Full-scale hydraulic performance of soil–bentonite and compacted clay liners. *Canadian Geotechnical Journal*, 39 (2), pp. 417–439.

Croney, D. (1977). The design and performance of road pavements. London: Her Majesty's Stationery Office.

Draft

593 Cui, Y. J., Loiseau, C. & Delage, P., (2002). Microstructure changes of a confined swelling soil due to suction controlled
594 hydration. In: *Unsaturated Soils. Proc. 3rd Int. Conf. on Unsaturated Soils (UNSAT 2002)*, Recife, Brazil (ed. Jucá, J.F.T.,
595 de Campos, T.M.P. and Marinho, F.A.M.), Lisse: Swets & Zeitlinger, Vol. 2, pp. 593-598.

596 Cuisinier, O., Auriol, J. C., Tangi, L. B. & Dimitri, D. (2011). Microstructure and hydraulic conductivity of a compacted
597 lime-treated soil. *Engineering Geology*, 123 (3), pp. 187–193

598 Cuisinier, O. & Masrouri, F. (2005). Hydromechanical behaviour of a compacted swelling soil over a wide suction range.
599 *Engineering Geology*, 81, 204–212.

600 Daniel, D. E. (1987). Earthen liners for land disposal facilities. *Geotech. Practice for Waste Disposal*. No. 13, R. D.
601 Woods, ed., Ann Arbor, Mich., 21–39.

602 Delage P. & Lefebvre G. (1984) Study of the structure of a sensitive Champlain clay and of its evolution during
603 consolidation. *Can. Geotech. J.*, 21, 1: 21–35.

604 Delage, P. & Pellerin, F.M. (1984). Influence de la lyophilisation sur la structure d'une argile sensible du Québec. *Clay*
605 *Minerals*, 19, 151-160.

606 Della Vecchia, G., Dieudonne, A. C., Jommi, C.& Charlier, R. (2015). Accounting for evolving pore size distribution in
607 water retention models for compacted clays. *International Journal for Numerical and Analytical Methods in*
608 *Geomechanics*, 39 (7), 702-723.

609 Della Vecchia, G., Jommi, C. & Romero E. (2013). A fully coupled elastic–plastic hydromechanical model for compacted
610 soils accounting for clay activity. *International Journal for Numerical and Analytical Methods in Geomechanics*, 37 (5),
611 503–535.

612 Drumm, E., Boles, D. & Wilson, G. (1997). Desiccation cracks result in preferential flow. *Geotech. News*, 152, 22–25.

613 Durner W (1994). Hydraulic conductivity estimation for soils with heterogeneous pore structure. *Water Resources*
614 *Research*, 30(2), 211–223

615 Eching, S. O. & Hopmans, J. W. (1993). Optimization of Hydraulic Functions from Transient Outflow and Soil Water
616 Pressure Data. *Soil Science Society of America Journal*, Vol. 57, pp. 1167–1175.

617 Fleureau J. M. , Verbrugge J. C. , Huergo P. J. , Correia A. G. , Kheirbek-Saoud S. (2002). Aspects of the behaviour of
618 compacted clayey soils on drying and wetting paths. *Canadian Geotechnical Journal,* 39:1341–1357.

619 Fredlund, D. G. & Rahardjo, H. (1993). Soil Mechanics for Unsaturated Soils. John Wiley & Sons, Inc., Hoboken, NJ,
620 USA. doi: 10.1002/9780470172759.ch1

621 Fujimaki, H. & Inoue, M. (2003). Reevaluation of the Multistep Outflow Method for Determining Unsaturated Hydraulic
622 Conductivity. *Vadose Zone Journal*, 2, pp. 409–415.

623 Gens, A. & Alonso, EE. (1992). A framework for the behaviour of unsaturated expansive clays. *Canadian Geotechnical*
624 *Journal*, 29, 1013–1032.

625 Iyer, B (1990) Pore water extraction – comparison of saturation extract and high-pressure squeezing. *Physico-chemical*
626 *Aspects of Soils and Related Materials – ASTM STP 1095 K.P. Hoddinot & R.O. Lamb (eds), Philadelphia,* 159-170

627 Jommi, C. (2000). Remarks on the constitutive modelling of unsaturated soils. In *Experimental Evidence and Theoretical*
628 *Approaches in Unsaturated Soils*, Tarantino A, Mancuso C (eds.). AA. Balkema: Rotterdam, 139–153.

629 Koliji, A., Vulliet, L. and Laloui, L. (2010). "Structural characterization of unsaturated aggregated soil". *Canadian*
630 *Geotechnical Journal*, 47(3): 297-297.

631 Leong, E., He, L. & Rahardjo, H. (2002). Factors Affecting the Filter Paper Method for Total and Matric Suction
632 Measurements. Geotechnical Testing Journal 25(3), 322-333.

633 Lloret, A., Villar, M. V., Sanchez, M., Gens, A., Pintado, X. & Alonso, E. E. (2003). Mechanical behaviour of heavily
634 compacted bentonite under high suction changes. Géotechnique, 53 (1), 27–40.

635 Mašín, D. (2013). Double structure hydromechanical coupling formalism and a model for unsaturated expansive clays.
636 *Engineering Geology*, 165, 73–88.

Draft

637 Mualem, Y. (1976). A new model for predicting the hydraulic conductivity of unsaturated porous media. Water Resources
638 Research, 12(3), 513–522.

639 Musso, G., Romero, E. & Della Vecchia, G. (2013). Double-structure effects on the chemo-hydromechanical behaviour
640 of a compacted active clay, *Géotechnique*, 15, 206-220.

641 Nocilla, A., Coop, M. R. & Colleselli, F. (2006). The mechanics of an Italian silt and example of "transitional" behaviour.
642 *Géotechnique*, 56, No. 4, 261-271.

643 Nowamooz, H.& Masrouri, F. (2009). Density-dependent hydromechanical behaviour of a compacted expansive soil.
644 *Engineering Geology*, 106, 105–115.

645 Rojas J.C, Mancuso C. and Danese D. (2010) Pre and post-construction characterization of an embankment fill material.
646 In *"Unsaturated soils. Experimental studies in unsaturated soils and expansive soils". Proceedings of the 4th Asia Pacific*
647 *conference on unsaturated soils*, Newcastle, Australia, 23-25 November 2009. Buzzi O. Fytus S. and Sheng D. editors,
648 CRC press.

649 Romero, E., Gens, A. & Lloret, A. (1999). Water permeability, water retention and microstructure of unsaturated
650 compacted Boom clay, Engineering Geology, 54, 117-127.

651 Romero, E. (2013). A microstructural insight into compacted clayey soils and their hydraulic properties. *Engineering*
652 *Geology*, 165, 3–19.

653 Romero, E., Della Vecchia, G. & Jommi, C. (2011). An insight into the water retention properties of compacted clayey
654 soils. *Géotechnique*, 61(4), 313–328.

655 Romero, E. & Jommi, C. (2008). An insight into the role of hydraulic history on the volume changes of anisotropic clayey
656 soils. *Water Resources Research*, 44, W12412:1–W12412:16.

657 Romero, E. & Vaunat, J. (2000). Retention curves of deformable clays. proc. int. workshop on unsaturated soils. In
658 Tarantino, A. and Mancuso, C., editors, *Experimental Evidence and Theoretical Approaches in Unsaturated Soils*, 91–
659 106, Trento, Italy. AA. Balkema, Rotterdam.

660 Romero, E., Vaunat, J. & Merchan V. (2014). Suction effects on the residual shear strength of clays. *Journal of Geo-*
661 *Engineering Sciences* 2 (2014) 17–37 DOI 10.3233/JGS-141320

662 Rouainia, M., Davies, O., O'Brien, T. & Glendinning, S. (2009). Numerical modelling of climate effects on slope stability.
663 *Proceedings of the Institution of Civil Engineers – Engineering Sustainability*, 162(2), 81–89.

664 Sharma, R. S. (1998). Mechanical behaviour of unsaturated highly expansive clays. PhD Thesis, Oxford University.

665 Smethurst, J. A., Clark, D. & Powrie, W. (2006). Seasonal changes in pore water pressure in a grass-covered cut slope in
666 London Clay. *Géotechnique*, 56 (8), 523-537.

667 Tarantino A, De Col S. (2008) Compaction behaviour of clay. Géotechnique, 58 (3):199–213.

668 U.S. Department of Agriculture (USDA) (1950). Diagnosis and improvement of saline and alkali soils, Agricultural
669 Handbook No. 60, USDA, Washington, DC.

670 van Dam, J. C., Stricker, J. N. M. & Droogers, P. (1994) Inverse Method to Determine Soil Hydraulic Functions from
671 Multistep Outflow Experiments. Soil Science Society of America Journal, Vol. 58, pp. 647– 652.

672 Van Genuchten, M. T. (1980). A closed-form equation for predicting the hydraulic conductivity of unsaturated soils. *Soil*
673 *Science Society of America Journal*, 44, 892–898.

674 Vassallo, R., Mancuso, C. & Vinale, F. (2007). Effects of net stress and suction history on the small strain stiffness of a
675 compacted clayey silt. *Canadian Geotechnical Journal*, 44(4), 447-462

676 Vaughan, P. R., Kovacevic, N. & Potts, D. M. (2004). Then and now: some comments on the design and analysis of
677 slopes and embankments. *Advances in Geotechnical Engineering: Proceedings of the Skempton Conference, Imperial*
678 *College*, London, Vol. 1, pp. 241–290.

679 Wang G., Wei X. (2015). Modeling swelling–shrinkage behavior of compacted expansive soils during wetting–drying
680 cycles. *Canadian Geotechnical Journal,* 52 (6), 783 – 79.

Draft

Wheeler, S. J., Sharma, R. S. & Buisson, M. S. R. (2003). Coupling of hydraulic hysteresis and stress-strain behaviour in unsaturated soils. *Géotechnique* 53(1), 41-54.

List of Tables

List of Figures

Draft

711 Figure 9. Hydromechanical model proposed to reproduce the behaviour of the peds: (a) Yield surfaces in σ'_m-s plane (b)
712 Influence of plastic strains on the water retention curve

713 Figure 10. Comparing model predictions and experimental data in terms void ratio and suction: (a) Total void ratio suction
714 (b) Evolution of e_{Ma} and e_m with suction

715 Figure 11. Comparing model predictions and experimental data in terms of S_r-log(s): (a) for the as-compacted specimen
716 (b) evolution of S_{rMa} and S_{rm} during repeated hydraulic loads (c) for the 6D/W specimen

717 Figure 12. Comparing model predictions and experimental data in terms of e_w-log(s) for: (a) as-compacted specimen
718 (b) 6D/W specimen

719 Figure 13. Hydraulic conductivity predicted by the proposed model: (a) k_r-S_e (b) K_w-S_e

720
721
722
723
724
725
726
727
728
729
730
731

Draft

Table 1. Properties of the tested soil

Variables	Value
Liquid limit *LL* (%)	32.6
Plastic limit *PL* (%)	24.3
Plasticity Index *PI* (%)	8.3
Activity *A* (-)	0.4
Specific Density G_s	2.735
Clay fraction (d<2μm, %)	20.4
$CaCO_3$ content (%)	17.3

Table 2. Properties of the as-compacted specimens

Condition	ρ_d (kg/m^3)	e (-)	w (%)	S_r (-)	s (kPa)
As-compacted	1650 ± 10	0.66 ± 0.01	20 ± 0.2	0.83 ± 0.02	33

Table 3. List of hydraulic and microstructural tests carried out with reference to figures

Type of test and figure	Method	Sample type
Water retention (Fig. 5)	Axis Translation, Vapour Equilibrium	As-compacted, 3D/W, 6D/W
Saturated hydraulic conductivity (Fig. 6, Fig. 14)	Constant head	As-compacted, 1D/W, 3D/W, 6D/W
Unsaturated hydraulic conductivity (Fig. 6, Fig. 14)	Back analysis of Richard's equation	As-compacted, 6D/W
Micro-photograph (Fig. 7)	Environmental Scanning Electron Microscopy	As-compacted, 6D/W
Pore Size Distribution and Pore Size Density (Fig. 8)	Mercury Intrusion Porosimetry	As-compacted, as compacted dry, 6D/W dry, 6D/W

Draft

Table 4. Threshold pore radii and micro-structural, meso-structural and macro-structural void ratios

void ratio	Lower threshold pore radius (nm)				Void ratio			
	As-compacted	First drying	6D/W dry	6D/W wet	As-compacted	First drying	6D/W dry	6D/W wet
e_{Mi}	-	-	-	-	0.06	0.06	0.06	0.06
e_{Me}	11	11	11	11	0.36	0.35	0.32	0.32
e_{Ma}	609	609	917	917	0.24	0.23	0.25	0.28
$e=e_{Ma}+e_{Me}+e_{Mi}$	-	-	-	-	0.66	0.64	0.63	0.66

Table 5. Parameters of the water retention model

Parameters	$1/\alpha_{Ma0}$ (kPa)	n_{Ma}	m_{Ma}	$1/\alpha_{m0}$ (kPa)	n_m	m_m
Drying	64	1.75	0.83	236	2.86	0.14
Wetting	8	2.37	0.97	34	2.61	0.12

Table 6. Parameters of the mechanical model

Parameters	κ	λ_m	h_{lC}	h_s	σ'^*_m kPa	s_I kPa	s_D kPa
Values	0.003	0.032	4.3	0.25	657	236	10

Draft

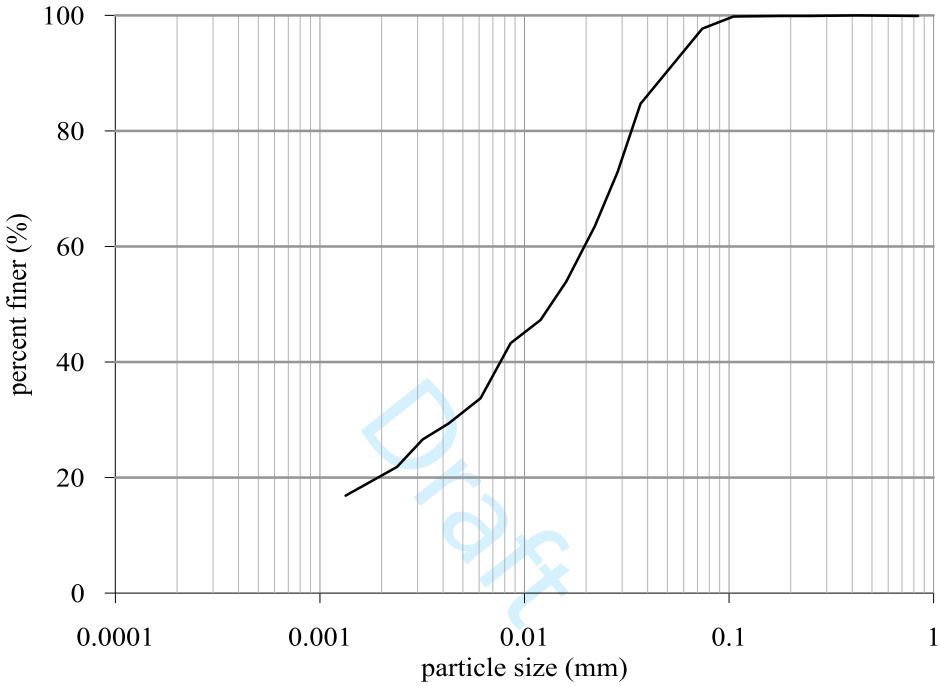

Figure 1. Grain size distribution of the tested material

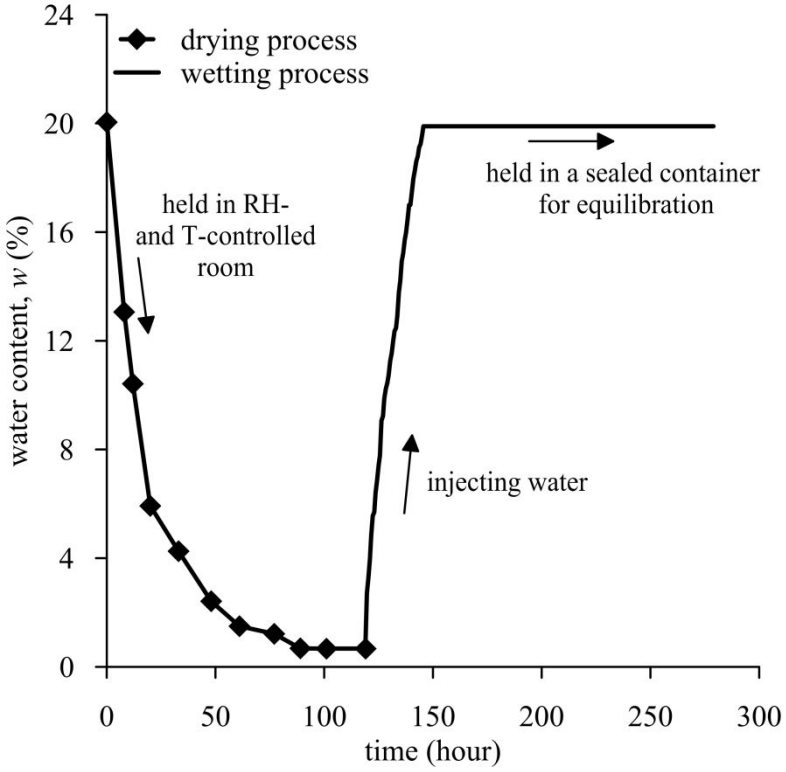

Figure 2. Water content changes during drying and wetting paths

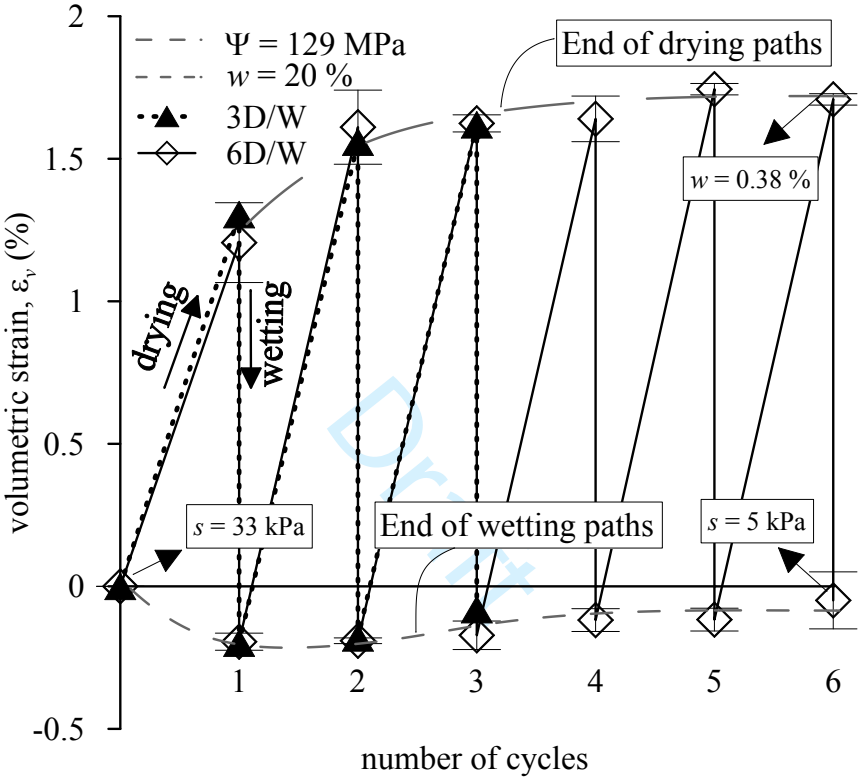

Figure 3. Mechanical response to repeated hydraulic loads: Volumetric strain with number of cycles

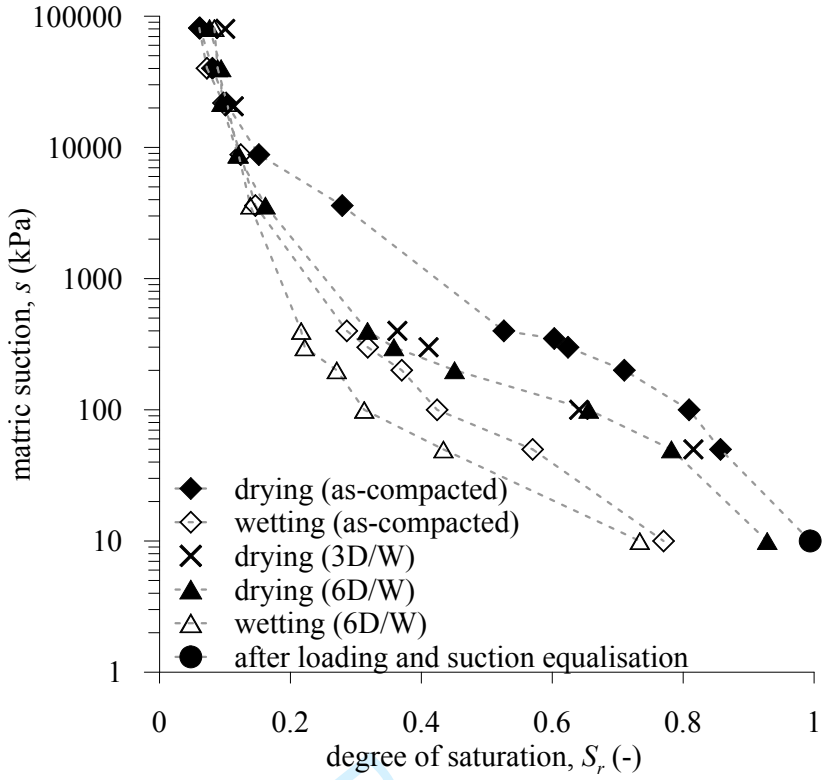
100000
10000
1000
100
10
1
matric suction, s (kPa)
drying (as-compacted)
wetting (as-compacted)
drying (3D/W)
drying (6D/W)
wetting (6D/W)
after loading and suction equalisation
0
0.2
0.4
0.6
0.8
1
degree of saturation, S_r (-)

(a)

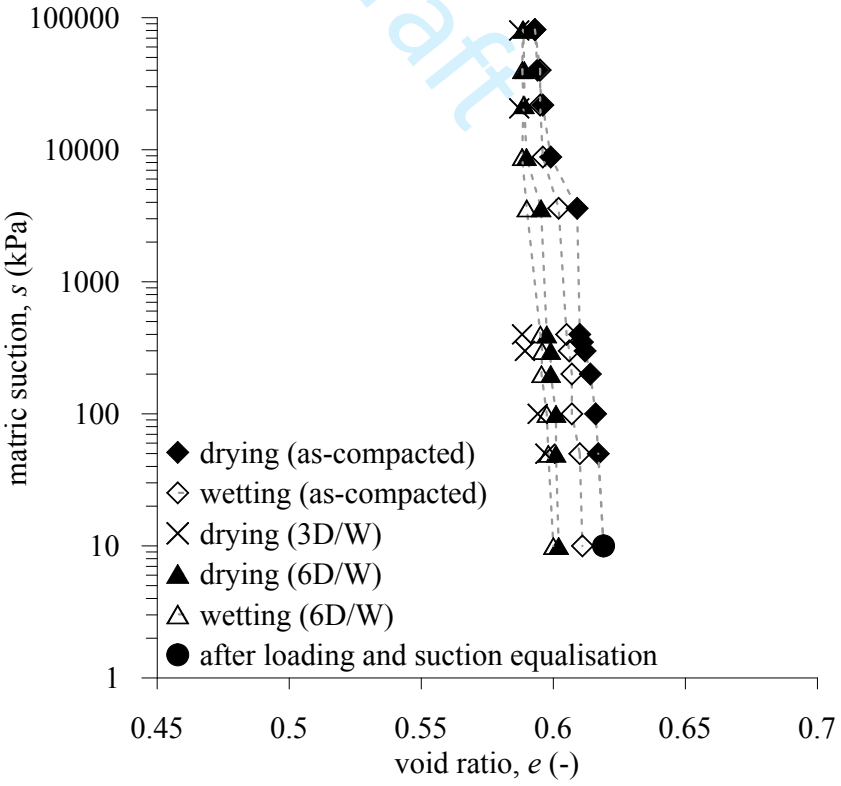
100000
10000
1000
100
10
1
matric suction, s (kPa)
drying (as-compacted)
wetting (as-compacted)
drying (3D/W)
drying (6D/W)
wetting (6D/W)
after loading and suction equalisation
0.45
0.5
0.55
0.6
0.65
0.7
void ratio, e (-)

(b)

Draft

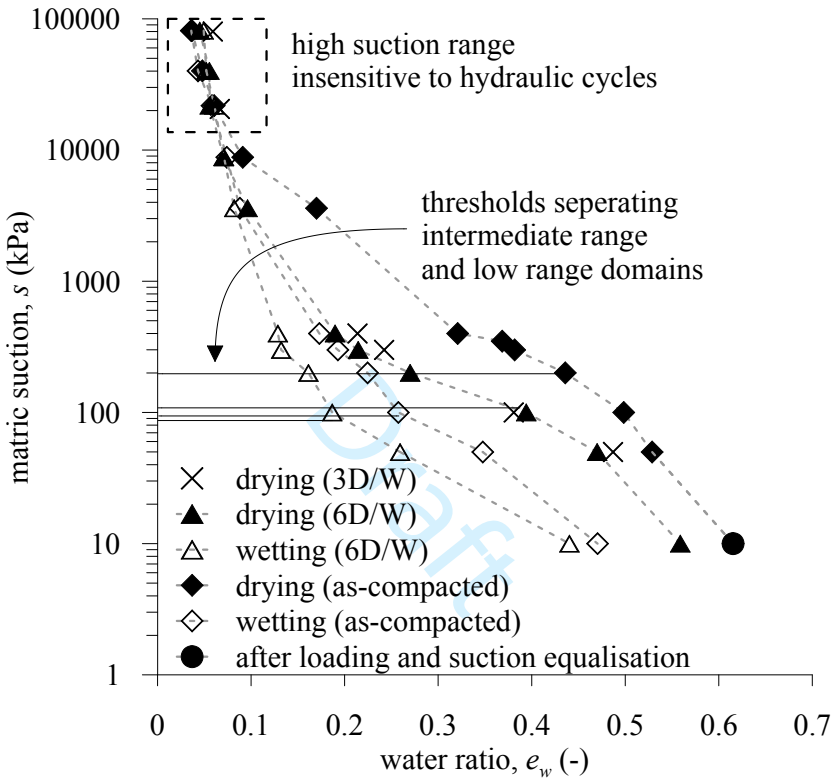

(c)

Figure 4. Effect of repeated hydraulic loads on the water retention behaviour: (a) S_r-log(s) (b) e-log(s) (c) e_w-log(s)

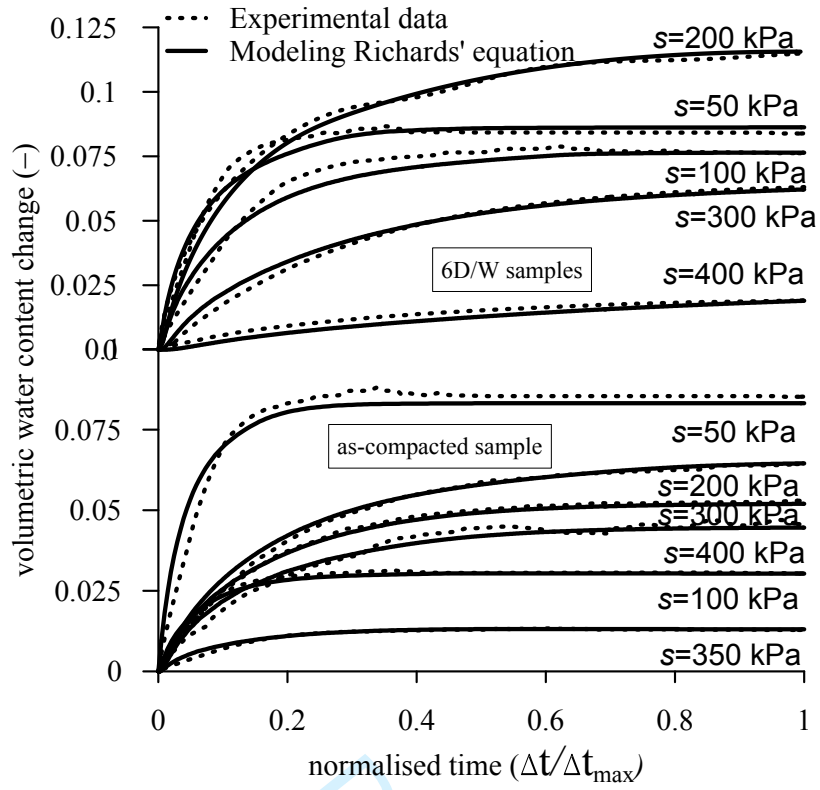

(a)

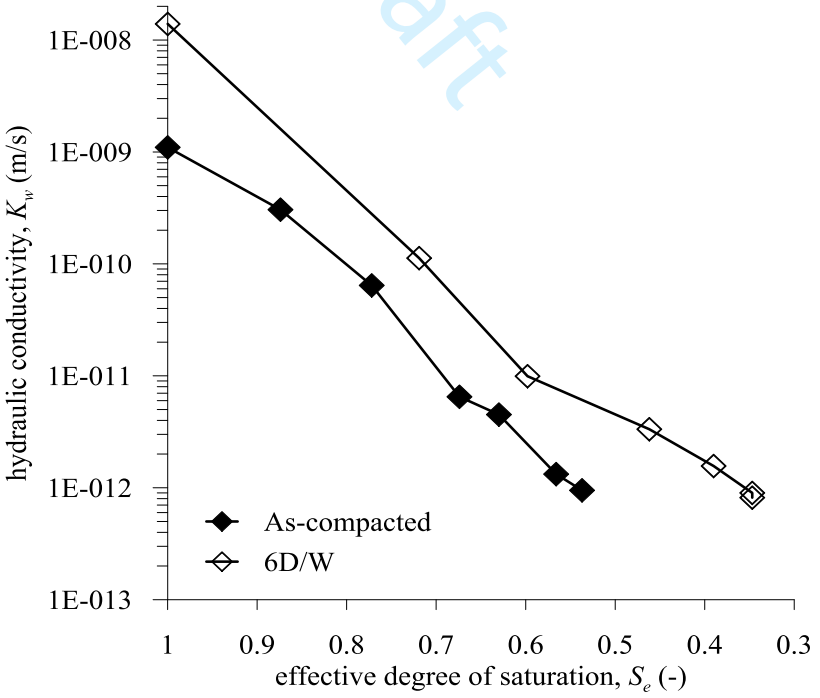

(b)

Figure 5. (a) Changes in volumetric water content: experimental data and inverse modeling (b) Unsaturated hydraulic conductivity of the as-compacted and 6D/W specimens

Draft

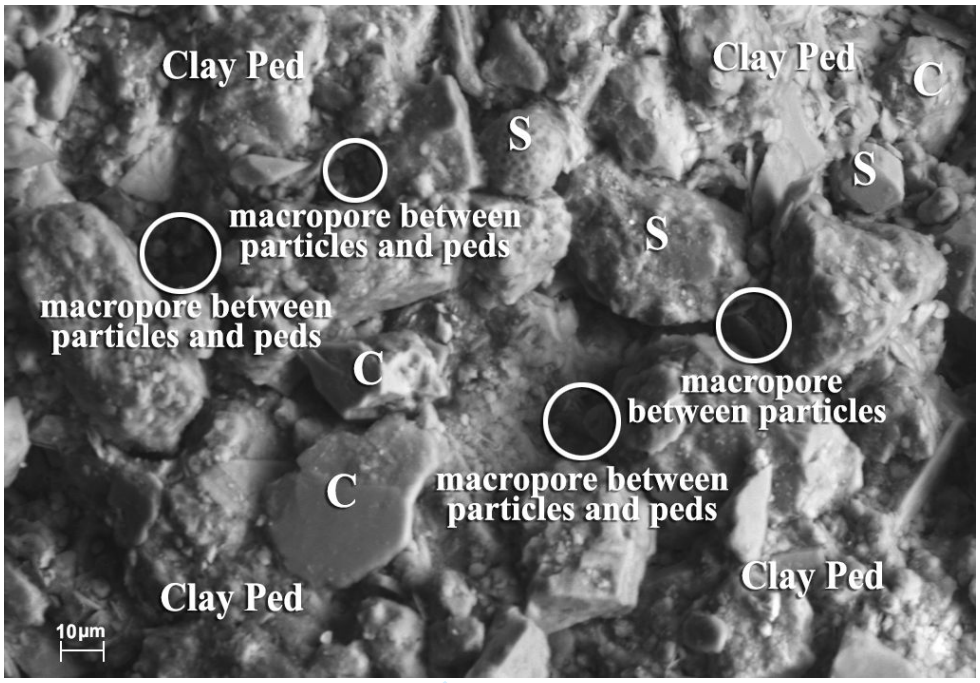
Clay Ped
Clay Ped
C
S
S
S
macropore between particles and peds
macropore between particles and peds
C
macropore between particles
C
macropore between particles and peds
Clay Ped
Clay Ped
10μm

(a)

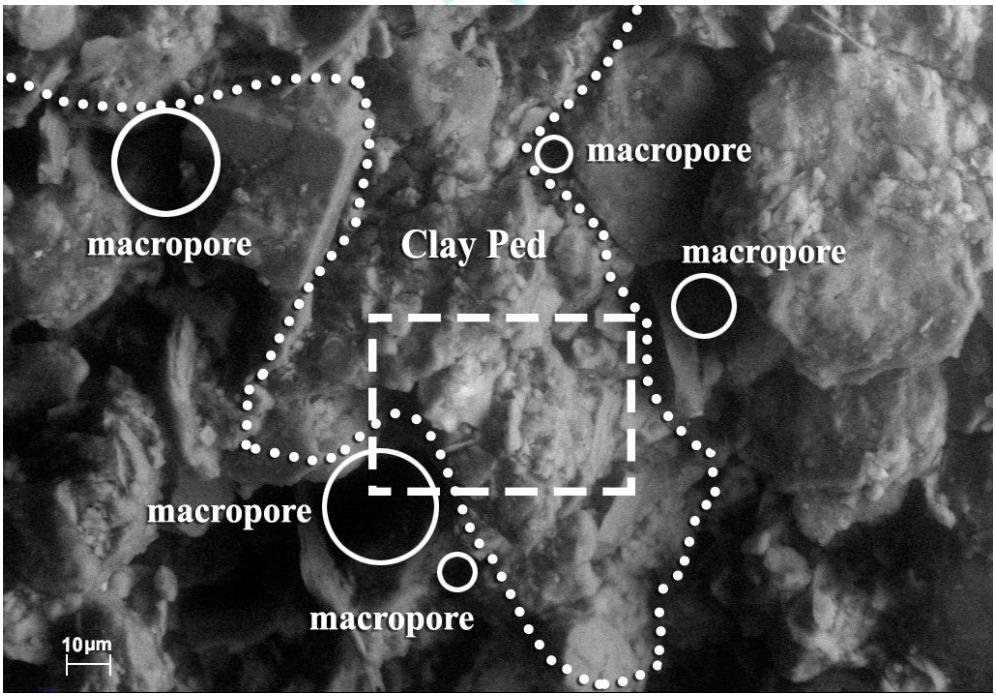
macropore
macropore
Clay Ped
macropore
macropore
macropore
10μm

(b)

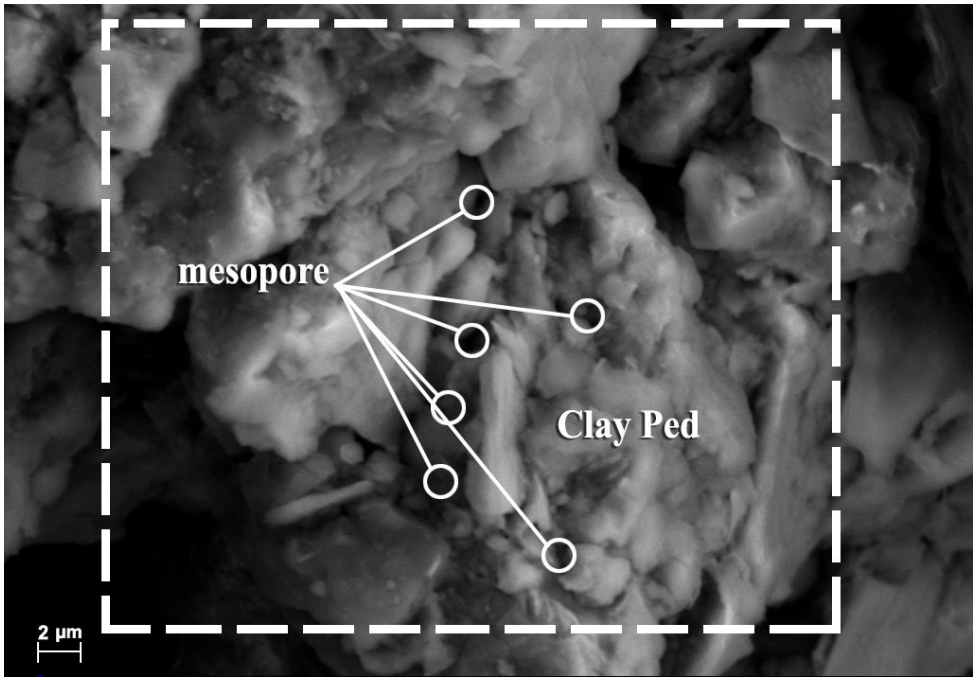

(c)

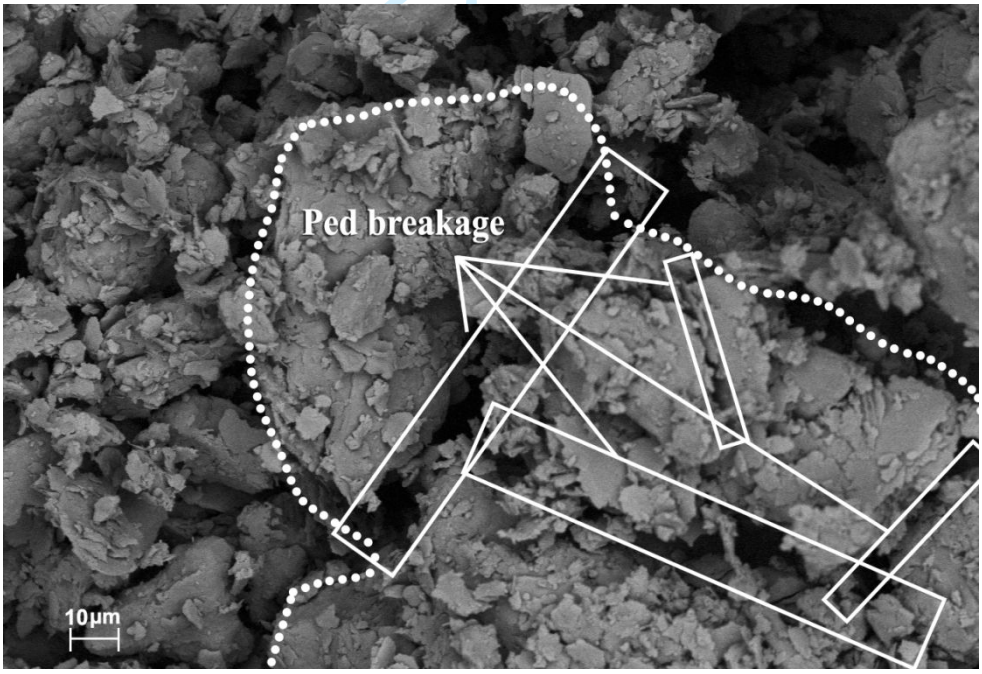

(d)

Figure 6. ESEM photomicrographs: (a) Particles, peds and macropores (b) Macropores and ped (c) Mesopores

(d) Ped breakage after drying-wetting cycles

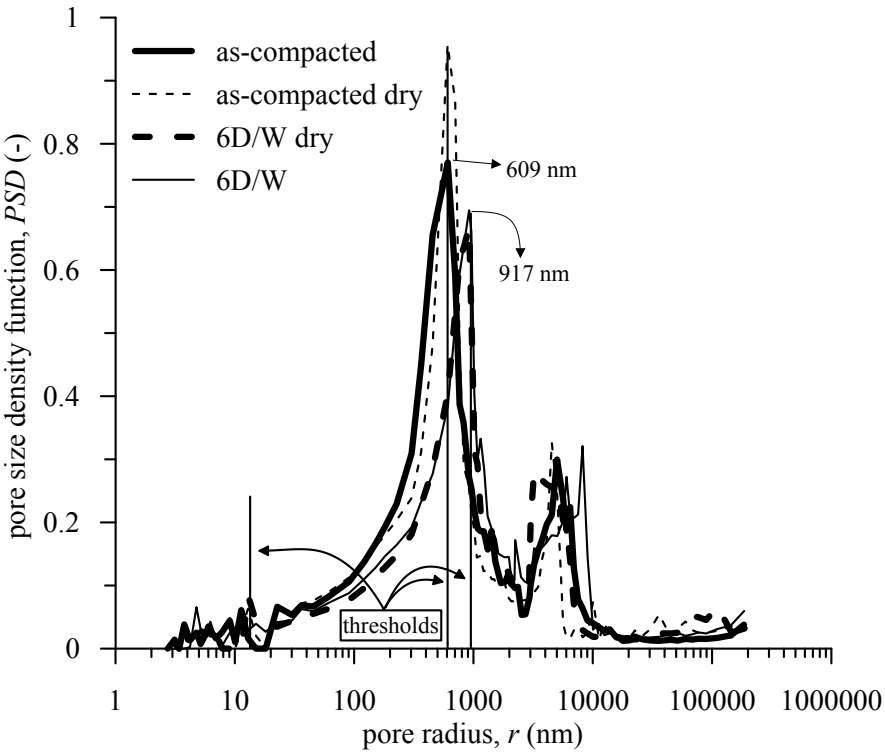

(a)

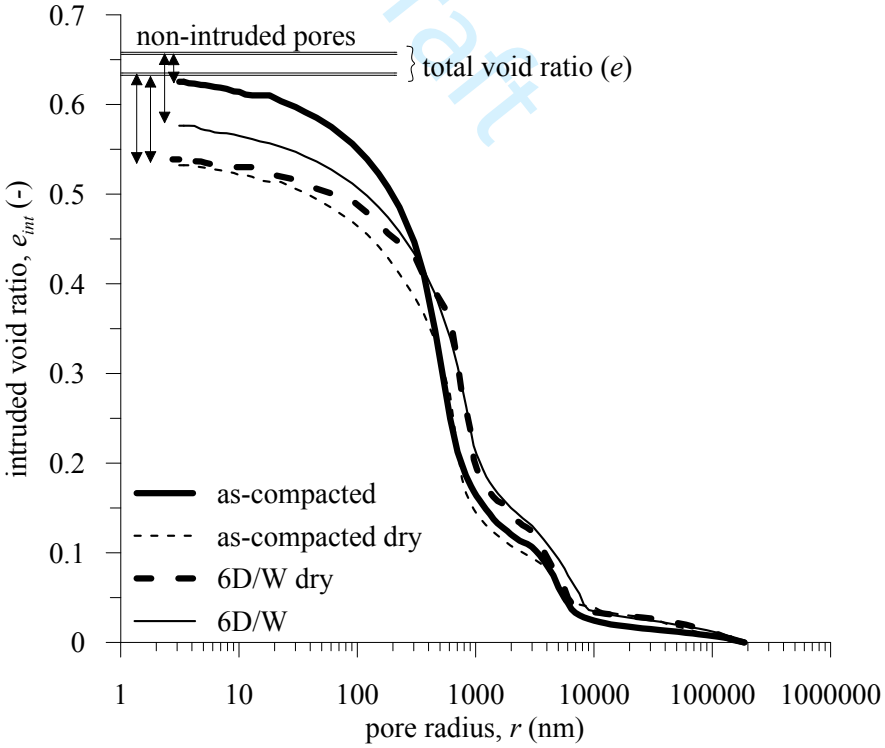

(b)

Figure 7. Effect of repeated hydraulic loads on MIP results: (a) Evolution of pore size density function (b) Evolution of intruded void ratio

Draft

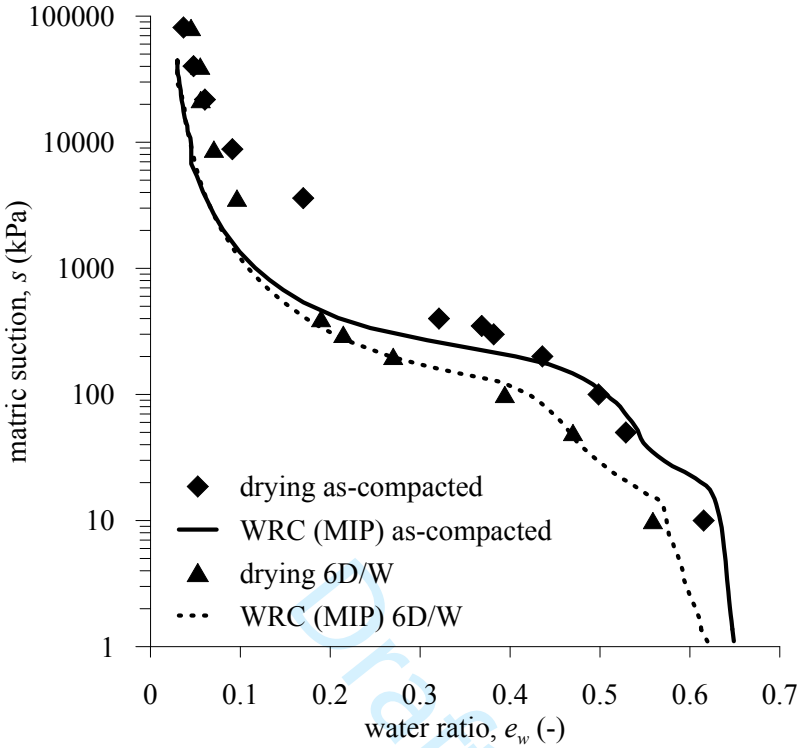

Draft

Figure 8. Comparison between the experimental and MIP derived WRCs

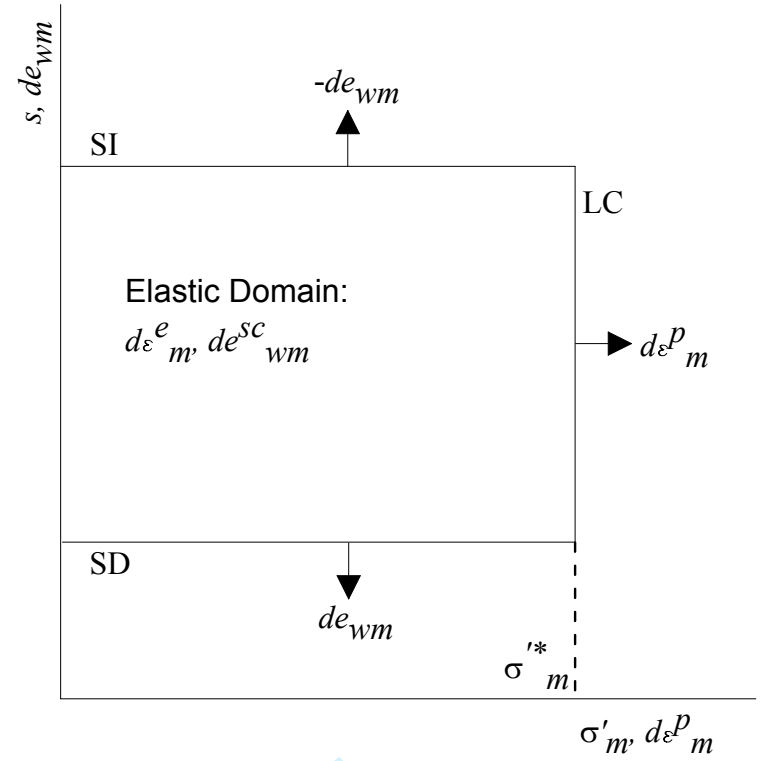

(a)

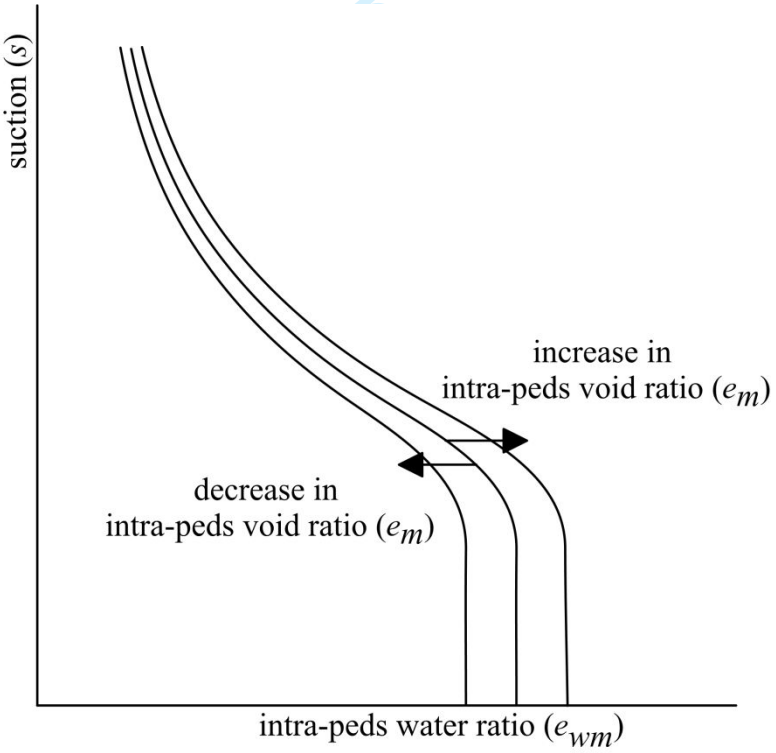

(b)

Figure 9. Hydromechanical model proposed to reproduce the behaviour of the peds: (a) Yield surfaces in σ'_m- s plane (b) Influence of plastic strains on the water retention curve

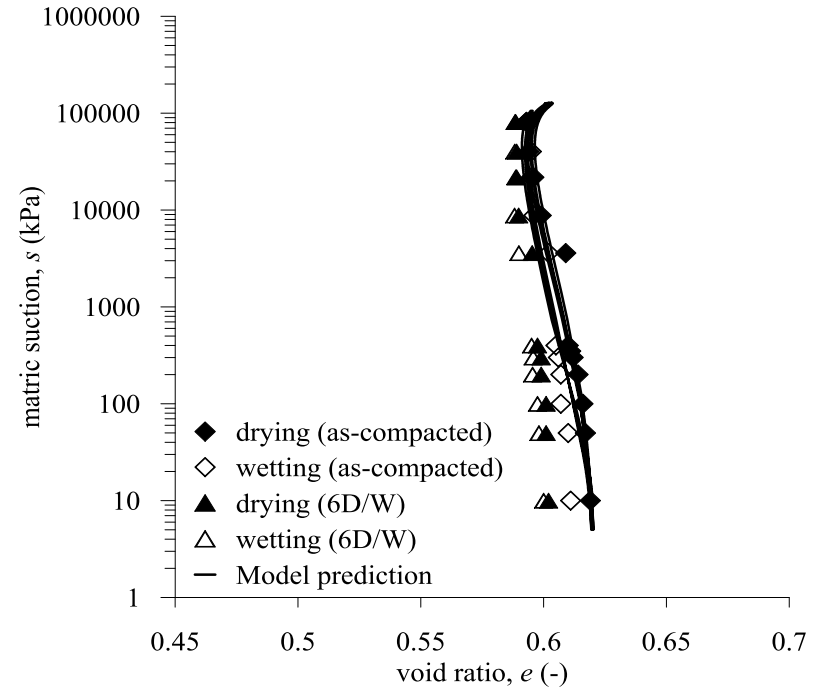

(a)

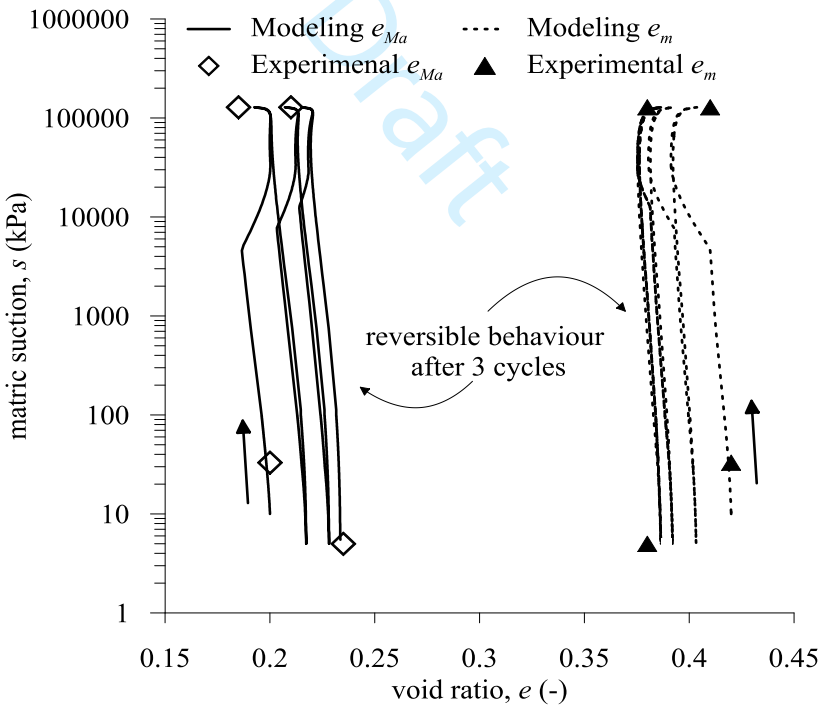

(b)

Figure 10. Comparing model predictions and experimental data in terms void ratio and suction: (a) Total void ratio suction (b) Evolution of e_{Ma} and e_m with suction

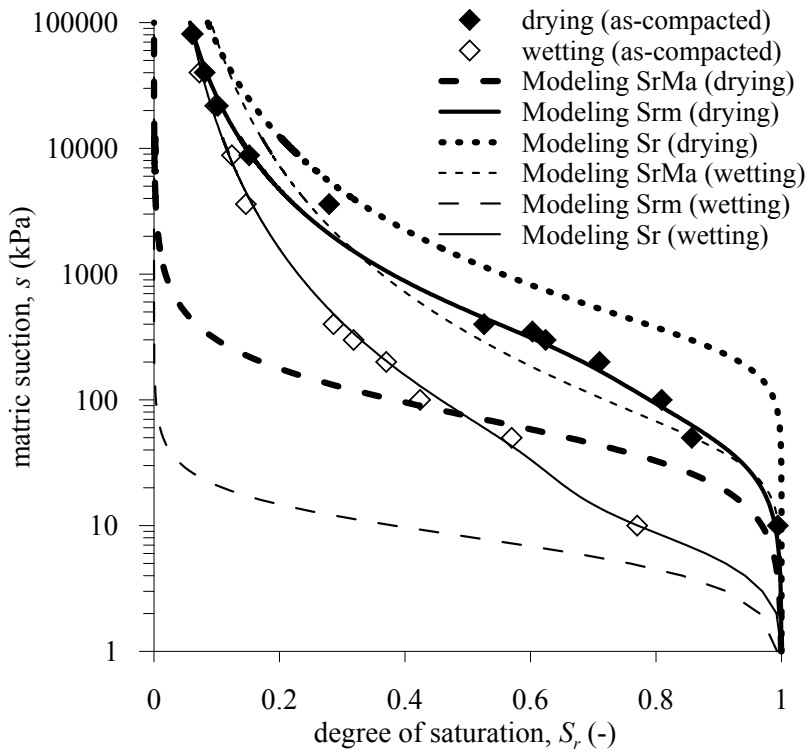
drying (as-compacted)
wetting (as-compacted)
Modeling SrMa (drying)
Modeling Srm (drying)
Modeling Sr (drying)
Modeling SrMa (wetting)
Modeling Srm (wetting)
Modeling Sr (wetting)
matric suction, s (kPa)
100000
10000
1000
100
10
1
0
0.2
0.4
0.6
0.8
1
degree of saturation, S_r (-)

(a)

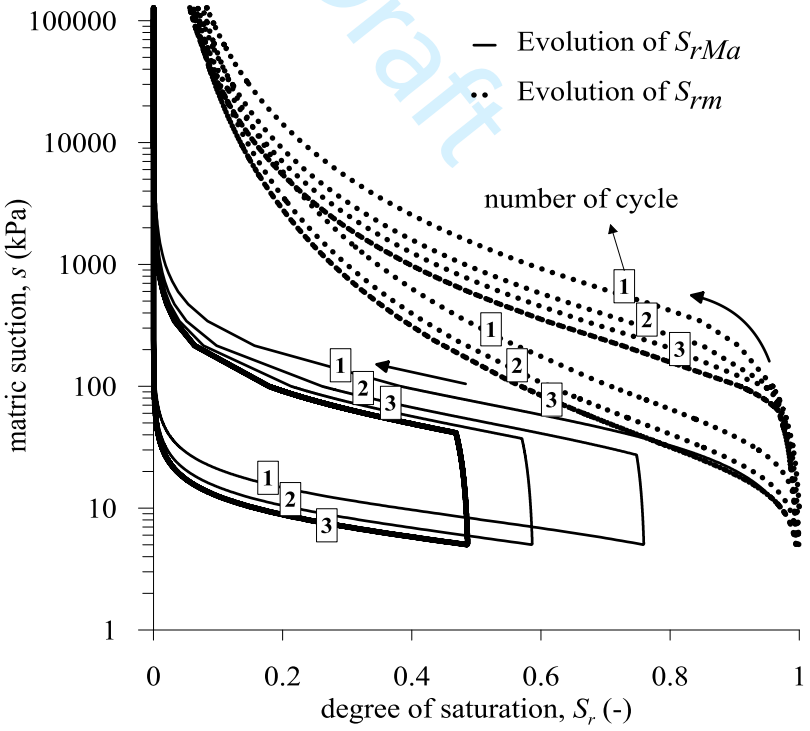
Evolution of S_{rMa}
Evolution of S_{rm}
number of cycle
1
2
3
matric suction, s (kPa)
100000
10000
1000
100
10
1
0
0.2
0.4
0.6
0.8
1
degree of saturation, S_r (-)

(b)

Draft

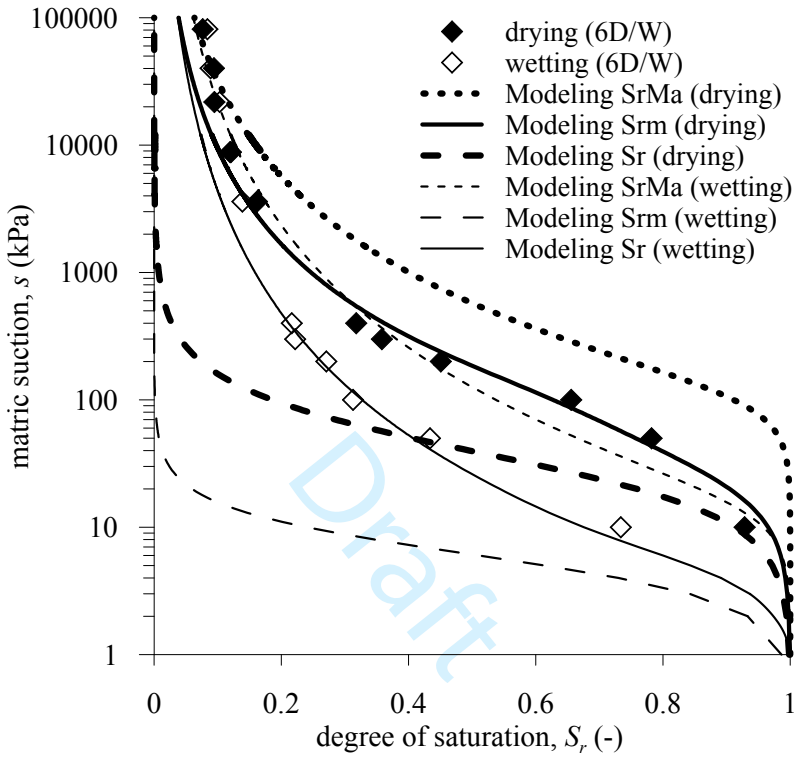

(c)

Figure 11. Comparing model predictions and experimental data in terms of S_r-log(s): (a) for the as-compacted specimen (b) evolution of S_{rMa} and S_{rm} during repeated hydraulic loads (c) for the 6D/W specimen

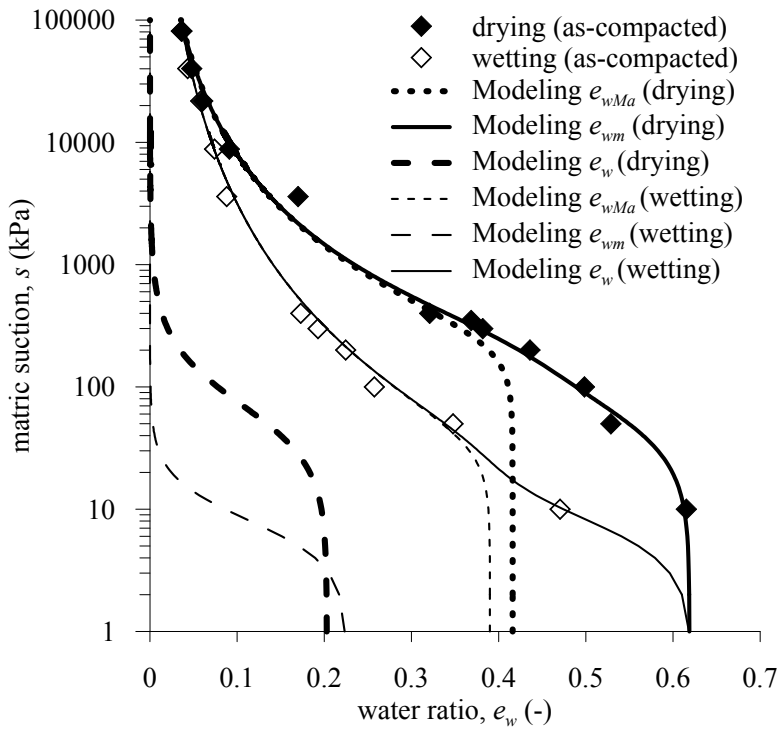

(a)

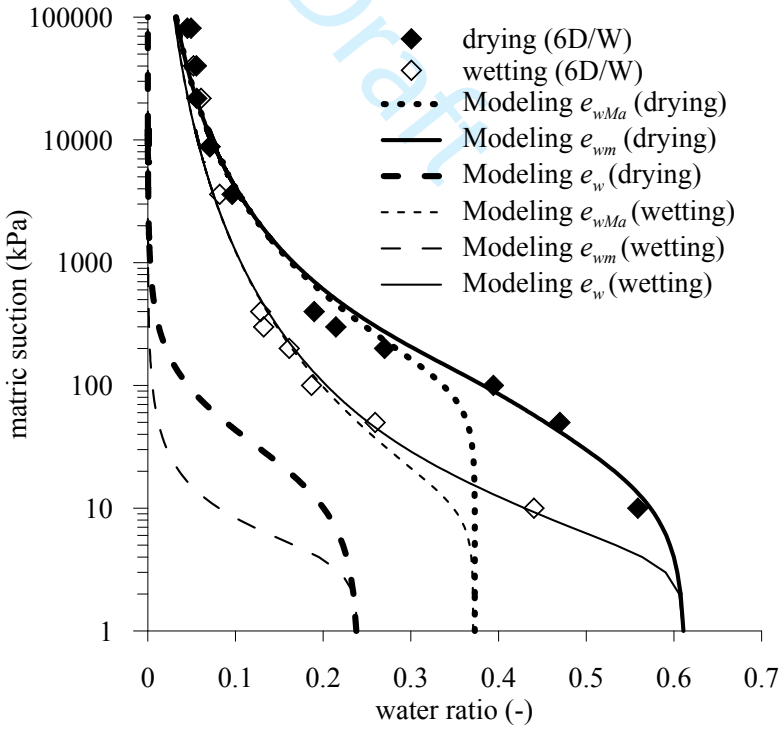

(b)

Figure 12. Comparing model predictions and experimental data in terms of e_w-log(s) for: (a) as-compacted specimen (b) 6D/W specimen

Draft

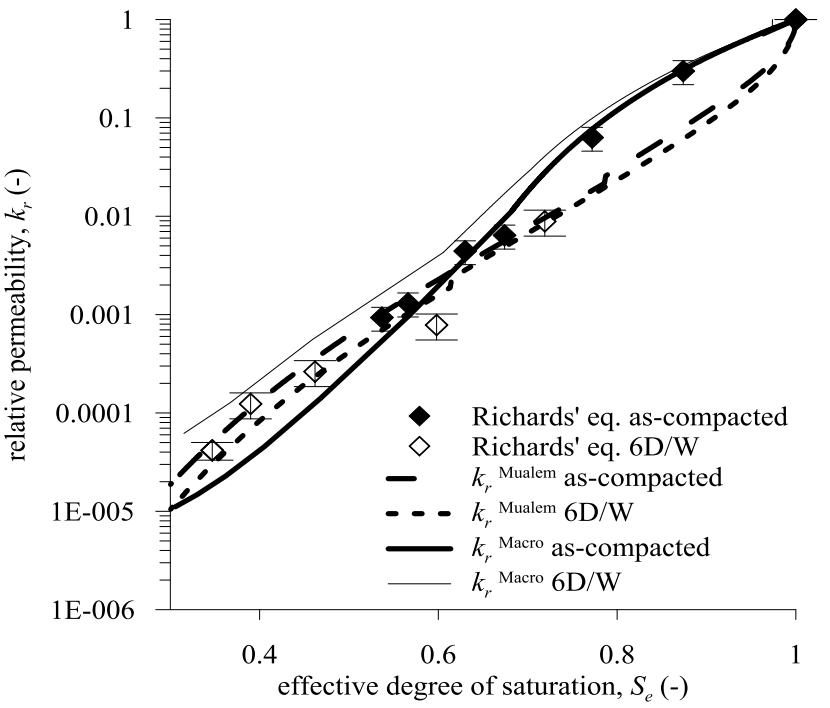

(a)

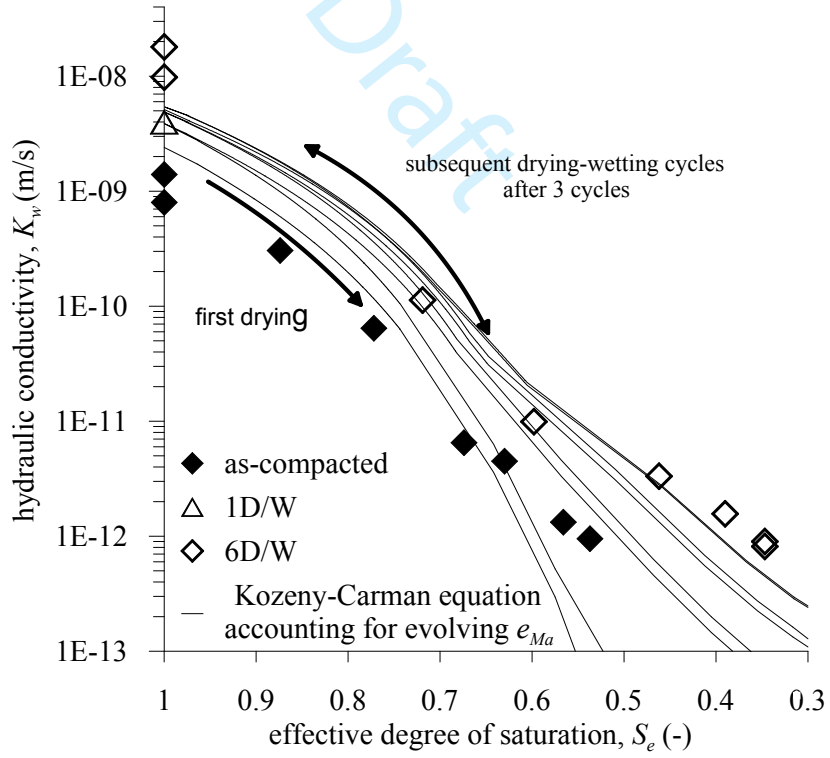

(b)

Draft

Figure 13. Permeability predicted by the proposed model: (a) k_r-S_e (b) K_w-S_e